National Defence / Défense nationale

2-D ACOUSTO-OPTIC SIGNAL PROCESSORS FOR SIMULTANEOUS SPECTRUM ANALYSIS AND DIRECTION FINDING (U)

by

Jim P.Y. Lee
RESM Section
Electronic Warfare Division

DEFENCE RESEARCH ESTABLISHMENT OTTAWA
REPORT NO.1049

PCN
011LB

November 1990
Ottawa

91-02794/

ABSTRACT

2–D Fourier transforming acoustooptic signal processors, for simultaneous direction finding (DF) and spectrum analysis of radar signals over a wide instantaneous bandwidth, are shown to be useful for Radar Electronic Support Measures (ESM) applications. A comprehensive treatment on the analysis and design of two general 2–D acoustooptic architectures is provided. In one architecture, a linear antenna array is employed, and in the other a novel circular antenna array with a Butler matrix beamformer is used. Emphasis is placed on the DF characteristics of both architectures. The effects of scaling factor, acoustic transducer height, Gaussian laser illumination profile , RF input noise, amplitude and phase tracking errors on the DOA pattern produced by each architecture are addressed. Design criteria and comparison between the two architectures are also provided.

RESUME

Les processeurs de signaux acoustooptiques opérant une transformée te Fourier bi–dimensionelle, pour l'analyze simultanée de l'angle d'arrivée et du spectre des signaux radars sur une bande instantanée large sont démontrés utiles pour des applications de mesures de soutien électroniques radar. Un traitement détaillé de l'analyze et de la conception de deux architectures accoustooptiques bi–dimensionelles générales est pourvu. Dans une des architectures, un étalage linéaire est employé et dans l'autre un nouvee étalage circulaire d'antennes avec un formeur de faisceau à matrice Butler est utilsé. L'emphase est placeé sur les caractéristiques de la mesure de l'angle d'arrivée des deux architectures. Les effets du facteur de démultiplication, de la hauteur du transducteur acoustique, du profile d'illumination gaussien du laser, du bruit d'entrée à frequence radioélectrique, et des erreurs de piste de l'amplitude et de la phase sur la courbe de l'angle d'arrivé produite par chaque architecture sont adressés. Les criteres de conception et une comparaison entre entre les deux architectures sont également pourvus.

EXECUTIVE SUMMARY

The increasing density and complexity of radar signals jeopardizes the capability of present day radar Electronic Support Measures (ESM) systems in sorting out specific emitters only on the basis of conventional signal parameters such as the radio frequency (RF), pulse repetition frequency (PRF) , pulse width (PW), amplitude ,etc.. Therefore, the separation of radar emitters on the basis of their bearing or direction of arrival (DOA) is of increasing importance. Moreover, there is increasing interest in higher bearing precision from radar ESM receivers to supplement radars and to place greater reliance on the use of passive sensors than active sensors. One of the promising receiver technologies which can provide simultaneously the frequency and bearing of radar signals over a wide instantaneous bandwidth is acoustooptics.

Optical signal processing is a fast–growing technology which is capable of handling large amounts of information in parallel and in two–dimensions. With the advent of new components such as Bragg cells and photodetector arrays, acoustooptic technology has rapidly emerged as a major optical processing technique for wide–band reception and analysis of radar signals. The most basic and best known 1–D acoustooptic receiver is the spectrum analyzer. This 1–D configuration can be extended to a 2–D one by the use of an antenna array and a multi–channel Bragg cell, in which the frequency spectrum of a received signal is provided in one dimension while its bearing is in the orthogonal one. This is indeed a very powerful signal sorting technique especially in a dense signal environment where the incoming signals may overlap. Accurate bearing and fine frequency measurements are obtained in this 2–D configuration, by combining the inherent high angular accuracy of an interferometer with the frequency spectral analysis capability of an acoustooptic spectrum analyzer.

There are two general 2–D acoustooptic architectures which have been analyzed in this report: one using a linear antenna array, and the other using a novel circular antenna array with a Butler matrix beamformer. Emphasis has been placed on the DF characteristics of both architectures. The effects of scaling factor, acoustic transducer height, laser illumination profile, RF input noise, amplitude and phase tracking errors on the DOA pattern produced by each of the 2–D acoustooptic architecture have been addressed. Design criteria and example for each architecture and a comparison between the two architectures have also been provided.

A typical example is presented to illustrate some optimization techniques on the design of a 2–D acoustooptic signal processor using a linear antenna array. It is shown that an aperiodic array configuration with a minimum of four to five channels is useful for broad–band receiver designs where it is required to cover an instantaneous angular field–of–view of one quadrant and with an angular accuracy of about one degree. This is based on factors such as complexity, cost, required main lobe beamwidth , sidelobe levels and antenna size constraint. However, the peak sidelobe–to–main–lobe level is usually high, –2 to –3 dB. In addition, the shift in the DOA pattern and DOA accuracy are scaled by a scaling factor.

The other approach in designing a 2–D acoustooptic signal processor is based on the circular antenna array with a Butler beamforming matrix. Some preliminary beamforming is carried out by the Butler matrix to couple the output from a circular antenna array to a multi–channel Bragg cell of a periodic arrangement. A typical example using a 32–element circular antenna array and a Butler matrix with 9 output ports has been given and a bearing accuracy of 1.5 degrees can be achieved. Some attractive features which can be identified when compared to the linear antenna array configuration are:

(i) A full 360–degree instantaneous field–of–view can be achieved using only one 2–D acoustooptic signal processor.

(ii) The shift and the shape of the DOA pattern are independent of input frequency, and as a result both the accuracy and resolution of this processor are also independent of frequency. Moreover the bearing accuracy is relatively insensitive to small elevation angle variations.

(iii) Due to periodic arrangement, the peak sidelobe–to–main–lobe level of the DOA pattern can be effectively reduced by the use of amplitude weighting.

In addition, the inter–transducer spacings can be reduced considerably and thus the through–put loss is less when the multi–channel Bragg cell is illuminated fully.

Despite the advantages associated with the circular antenna array configuration ,the aperiodic linear array configuration does offer some good features. For the same number of channels, an aperiodic arrangement can provide a longer baseline and all those attractive features associated with it, such as better bearing accuracy. There may be lower cross–talks among those channels further apart. In addition the microwave front–end will be less complicated and much smaller in size which will result in a lower cost. However when the elevation angle is not zero ,the bearing accuracy will deteriorate due to "Coning" angle problems.

The ultimate choice depends on the system requirement. The circular array configuration can provide a system which is more compact if the full 360–degree instantaneous field–of–view is required. The bearing accuracy is moderate, on the order of 1 degree with a 9–channel system. For angular accuracy of better than 1 degree, the linear array configuration is a better choice if the errors associated with the "Coning" angle can be solved by either measuring the elevation angle using another system or by operating the system for very low elevation coverage.

TABLE OF CONTENTS

		PAGE
ABSTRACT/RESUME		iii
EXECUTIVE SUMMARY		v
TABLE OF CONTENTS		vii
LIST OF FIGURES		ix
LIST OF TABLES		xv
LIST OF PRINCIPAL ABBREVIATIONS AND SYMBOLS		xvii
1.0	INTRODUCTION	1
2.0	FOURIER TRANSFORMING CONFIGURATION	3
3.0	USE OF BRAGG CELLS AS SPATIAL LIGHT MODULATORS	5
4.0	2–D ACOUSTOOPTIC FOURIER TRANSFORMING PROCESSORS	7
4.1	Processor Architecture Employing A Linear Antenna Array	8
4.2	Processor Architecture Using A Circular Antenna Array And A Butler Matrix	12
5.0	SCALING FACTOR (S.F.)	15
6.0	EFFECT OF TRANSDUCER HEIGHT ON DOA PATTERN	18
7.0	GAUSSIAN LASER ILLUMINATION PROFILE	19
7.1	DOA Main Lobe Intensity Versus Gaussian Profile Parameter Ty	21
8.0	ERROR TOLERANCE ANALYSIS	21
8.1	Optical Array Pattern	21
8.2	RMS Beam–Pointing Error	23
9.0	EFFECT OF NOISE ON DETECTED DOA PATTERN	26
9.1	Single–channel Bragg Cell Configuration	27
9.2	Multi–channel Bragg Cell Configuration	33
10.0	COMPARISON BETWEEN MICROWAVE AND OPTICAL ARRAY PATTERNS	36

TABLE OF CONTENTS (cont.)

		PAGE
11.0	DESIGN CRITERIA USING A LINEAR ANTENNA ARRAY	36
11.1	Linear Periodic Array Versus Aperiodic Array	36
11.2	Design Example	37
12.0	DESIGN CRITERIA USING A CIRCULAR ANTENNA ARRAY WITH A BUTLER MATRIX	48
13.0	COMPARISON BETWEEN THE TWO CONFIGURATIONS	55
14.0	SUMMARY AND CONCLUSIONS	62
15.0	REFERENCES	65
APPENDIX	DERIVATION OF RMS BEAM–POINTING ERROR FOR 2–D ACOUSTOOPTIC SIGNAL PROCESSOR	69

LIST OF FIGURES

		PAGE
FIGURE 1:	TWO–DIMENSIONAL ACOUSTOOPTIC RECEIVER	2
FIGURE 2:	FOURIER TRANSFORMING CONFIGURATION	4
FIGURE 3:	LINEAR ANTENNA ARRAY CONFIGURATION	9
FIGURE 4:	MULTI–CHANNEL BRAGG CELL CONFIGURATION	11
FIGURE 5:	CIRCULAR ANTENNA ARRAY AND FEED NETWORK	13
FIGURE 6:	PHASE IN THE FAR FIELD VERSUS BEARING ANGLE	14
FIGURE 7:	TWO–DIMENSIONAL ACOUSTOOPTIC RECEIVER USING A CIRCULAR ANTENNA ARRAY AND A BUTLER MATRIX	16
FIGURE 8:	NORMALIZED OUTPUT SIGNAL–TO–NOISE RATIO VERSUS INPUT SIGNAL–TO–NOISE RATIO (a) ——— $(x_{ij} - x_{is}, y_i)/ \mathcal{H}^2(0,y_i) = 1.0$ (b) ····· $(x_{ij} - x_{is}, y_i)/ \mathcal{H}^2(0,y_i) = 0.5$ (c) –·–·– $(x_{ij} - x_{is}, y_i)/ \mathcal{H}^2(0,y_i) = 0.25$ (d) – – – – $(x_{ij} - x_{is}, y_i)/ \mathcal{H}^2(0,y_i) = 0.125$	32
FIGURE 9:	NORMALIZED INTENSITY PATTERN OF AN OPTIMUM APERIODIC ARRAY [Base line = 10.5 λ_R at 12.5 GHz; Element locations(λ_R): –5.25, –1.54, 0.98, and 5.25, H = $\ell_N/30$]	44
FIGURE 10:	TOTAL INTERACTING OPTICAL INTENSITY AND ITS PEAK DOA INTENSITY VERSUS TY FOR AN OPTIMUM APERIODIC ARRAY (a) Total Optical Intensity Utilized in the Interaction with Acoustic Beams (b) Relative Peak Intensity of DOA Pattern	46
FIGURE 11:	NORMALIZED DOA PATTERN OF AN OPTIMUM 4–CHANNEL APERIODIC ARRAY ILLUMINATED WITH (a) ——— Rectangular Weighting (b) ····· Optimum Gaussian Weighting (Ty = 0.8)	47
FIGURE 12:	NORMALIZED DOA PATTERN OF A 9–CHANNEL RECEIVER USING A CIRCULAR ANTENNA ARRAY (a) ——— Ty = 0, $H/\ell = 0.2$ (b) ····· Ty = 0.88, $H/\ell = 0.2$	49

PAGE

FIGURE 13: TOTAL INTERACTING OPTICAL POWER VERSUS Ty FOR A N–CHANNEL RECEIVER USING A CIRCULAR ANTENNA ARRAY ($H/\ell = 0.2$) 50

FIGURE 14: RELATIVE PEAK INTENSITY OF DOA PATTERN VERSUS Ty FOR A N–CHANNEL RECEIVER USING A CIRCULAR ANTENNA ARRAY ($H/\ell = 0.2$) 51

FIGURE 15: 3–dB BEAMWIDTH VERSUS Ty FOR A N–CHANNEL RECEIVER USING A CIRCULAR ANTENNA ARRAY ($H/\ell = 0.2$) 53

FIGURE 16: PEAK SIDELOBE LEVEL VERSUS Ty FOR A N–CHANNEL RECEIVER USING A CIRCULAR ANTENNA ARRAY ($H/\ell = 0.2$) 54

FIGURE 17: RATIO OF 3–dB BEAMWIDTH POWER TO TOTAL POWER VERSUS Ty FOR A N–CHANNEL RECEIVER USING A CIRCULAR ANTENNA ARRAY ($H/\ell = 0.2$) 55

FIGURE 18: P.F VERSUS Ty FOR A N–CHANNEL RECEIVER USING A CIRCULAR ANTENNA ARRAY ($H/\ell = 0.2$) 57

FIGURE 19: NORMALIZED DOA PATTERN OF A 9–CHANNEL RECEIVER USING A CIRCULAR ANTENNA ARRAY FOR Ty = 0 and $H/\ell = 0.2$ 58
(a) ——— Error Free
(b) ····· 30° RMS Phase Error, –3 dB RMS Power Error
(c) - - - - - 15° RMS Phase Error, –6 dB RMS Power Error
(d) —·—·— 7.5° RMS Phase Error, –9 dB RMS Power Error

FIGURE 20: NORMALIZED DOA PATTERN OF A 9–CHANNEL RECEIVER USING A CIRCULAR ANTENNA ARRAY FOR OPTIMUM Ty = 0.88 and $H/\ell = 0.2$ 59
(a) ——— Error Free
(b) ····· 30° RMS Phase Error, –3 dB RMS Power Error
(c) - - - - - 15° RMS Phase Error, –6 dB RMS Power Error
(d) —·—·— 7.5° RMS Phase Error, –9 dB RMS Power Error

FIGURE 21: NORMALIZED DOA PATTERN OF A RECEIVER USING A CIRCULAR ANTENNA ARRAY FOR Ty = 0.88 and $H/\ell = 0.2$ 60
(a) ——— 9–channel Filled Array
(b) ····· 7–channel Thinned Array

LIST OF TABLES

		PAGE
TABLE I:	OPTIMUM TABLE SHOWING THE PEAK SIDELOBE –TO–MAIN–LOBE VALUES FOR AN ARRAY OF 10.5 WAVELENGTHS LONG	39
TABLE II:	OPTIMUM TABLE SHOWING THE PEAK SIDELOBE– TO–MAIN–LOBE VALUES FOR AN ARRAY OF 10.5 WAVELENGTHS LONG	40
TABLE III:	OPTIMUM TABLE SHOWING THE PEAK SIDELOBE– TO–MAIN–LOBE VALUES FOR AN ARRAY OF 10.625 WAVELENGTHS LONG	41
TABLE IV:	OPTIMUM TABLE SHOWING THE PEAK SIDELOBE– TO–MAIN–LOBE VALUES FOR AN ARRAY OF 10.3125 WAVELENGTHS LONG	42

LIST OF PRINCIPAL ABBREVIATIONS AND SYMEOLS

n	Amplitude of channel n
B_η	Equivalent noise bandwidth of photodetector
CW	Continuous wave
D	Aperture width of Bragg cell
d_n	Location of antenna element n
DOA	Direction of arrival
F	Focal length
f_R	RF frequency
f(v)	Normalized optical array pattern function
f_s	Acoustic frequency
H	Height of acoustic transducer
$H(x_1,y_1)$	Spatial weighting function of detector
IF	Intermediate frequency
k	Optical phase constant
K_B^2	Acoustooptic diffraction efficiency of Bragg cell
L	Length of acoustic transducer
P.F.	Proportionality Factor
S.F.	Scaling Factor
T	Integration time of photodetector array
Tx, Ty	Gaussian laser beam profile parameters in the x_1 and y_1 axes respectively
(u,v)	Spatial frequency components corresponding to x_1 and y_1 axes respectively

LIST OF PRINCIPAL ABBREVIATIONS AND SYMBOLS (cont)

v_s	Acoustic phase velocity
$w(x_o,y_o)$	Amplitude window weighting function
(x_o,y_o)	Coordinates of Bragg cell
(x_1,y_1)	Fourier plane coordinates
a	Acoustic loss coefficient
β_n	Phase delay of channel n
θ	Angle of arrival
Λ	Acoustic wavelength
λ	Optical wavelength
λ_R	RF wavelength
ϕ_o	Electrical phase angle
τ	Transit time across Bragg cell aperture
τ'	Time delay
ω	Optical angular frequency
ℓ_n	Location of acoustic transducer n

1.0 INTRODUCTION

The increasing density and complexity of radar signals jeopardizes the capability of present day radar Electronic Support Measures (ESM) systems in sorting out specific emitters only on the basis of conventional signal parameters such as the radio frequency (RF), pulse repetition frequency (PRF) , pulse width (PW), amplitude ,etc.[1]. Therefore, the separation of radar emitters on the basis of their bearing or direction of arrival (DOA) is of increasing importance. Moreover, there is increasing interest in higher bearing precision from radar ESM receivers to supplement radars and to place greater reliance on the use of passive sensors than active sensors [1]. As a result, it is highly desirable to develop a wide band radar ESM receiver where the incoming signals can be sorted out instantaneously and accurately in terms of frequency and direction of arrival under signal overlapping conditions.

Optical signal processing is a fast–growing technology which is capable of handling large amounts of information in parallel and in two dimensions. Operations such as Fourier transformation, correlation or convolution are performed at a rate limited only by the characteristics of the input and output devices. With the advent of components such as Bragg cells and photodetector arrays, acoustooptic technology has rapidly emerged as a major optical signal processing technique. Many architectural optical signal processors have been developed [2] and the Fourier transforming configuration is the most significant and best known.

One of the key applications of the Fourier transformation configuration is in the development of radar ESM receivers. The most basic and best known one–dimensional (1–D) acoustooptic Fourier transforming configuration is the spectrum analyzer[3–4]. This 1–D configuration can be extended to a two–dimensional (2–D) one, in which the frequency spectrum of a received signal is provided in one dimension and its DOA is in the orthogonal dimension. Thus the requirement of measuring simultaneously the DOA and frequency spectrum of a received signal can be accomplished with a 2–D Fourier transforming configuration employing a multi–channel Bragg cell [5–8]. A block diagram of one of these 2–D acoustooptic receiver architectures is shown in Fig.1, where a linear antenna array is used to intercept incoming radar signals[8]. A signal received by each antenna element is down–converted to an intermediate frequency (IF) signal. The IF signals are then applied to a multi–channel Bragg cell where the relative acoustic transducer spacings are the same as those of the antenna array. Through the process of acoustooptic diffraction, the acoustic signals are coherently processed in parallel to produce optically a 2–D Fourier transform of the signals in the Fourier plane. The intensity distribution of this Fourier transform gives the power spectrum of the signal on one axis and its DOA or bearing on the other. This is indeed a very powerful signal sorting technique in which the incoming signals are spatially separated in frequency and DOA. Accurate DOA and fine frequency measurements are obtained in this configuration, by combining the inherent high angular accuracy of an interferometer with the frequency spectral analysis capability of an acoustooptic spectrum analyzer. The instantaneous angular field–of–view of this architecture when using a linear antenna array is restricted to less than 180 degrees. Thus in order to achieve a complete angular coverage of 360 degrees , a number of processors are needed. A different, novel approach for covering an instantaneous 360–degree field–of–view consists of a circular antenna array with a Butler matrix beamformer [9]. The acoustic transducer array on the multi–channel Bragg cell in such an architecture is of a periodic arrangement.

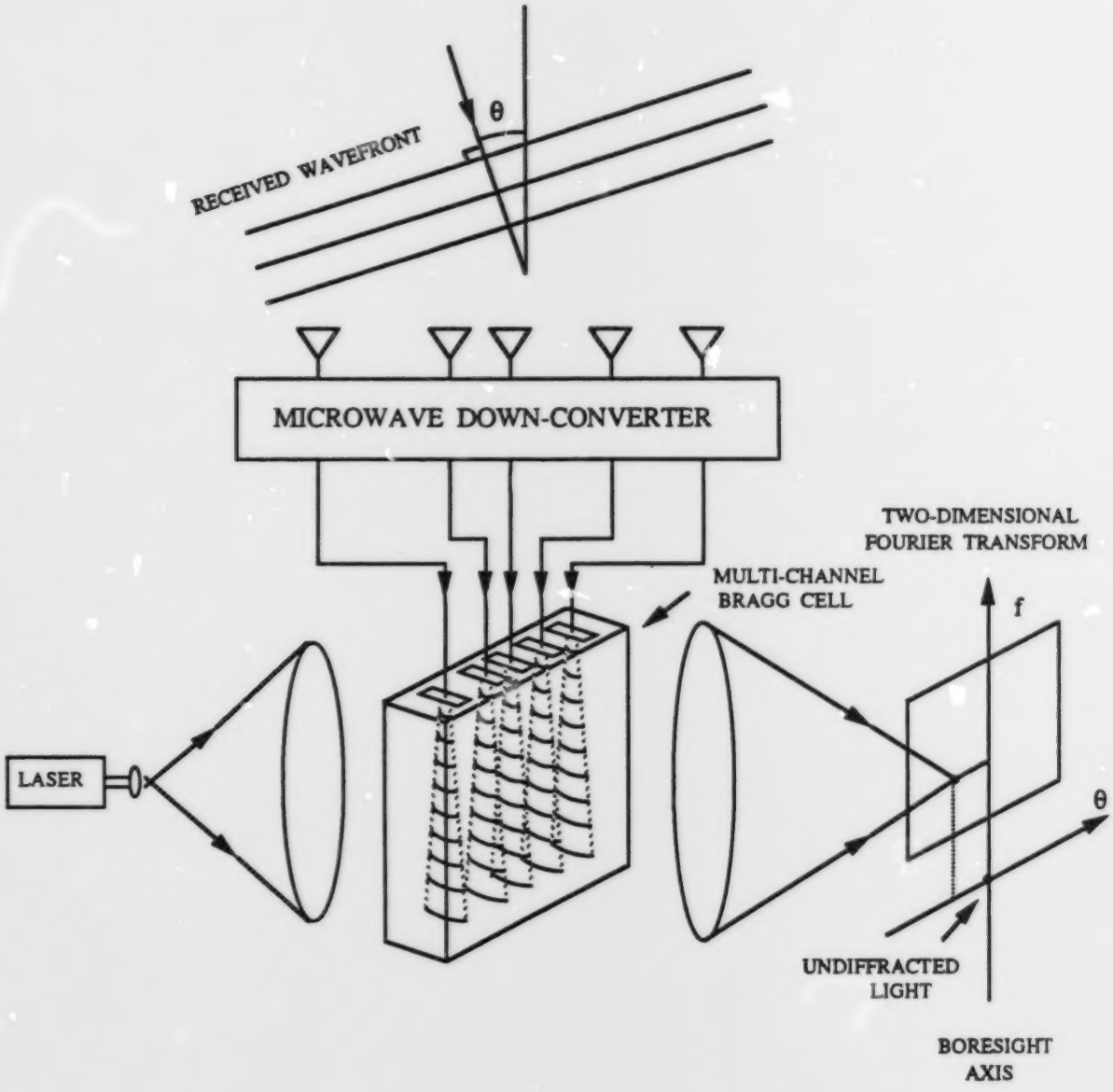

FIGURE 1: TWO–DIMENSIONAL ACOUSTOOPTIC FOURIER TRANSFORMING SIGNAL PROCESSOR

In this report, a general formulation on the Fourier transforming configuration is presented. This formulation is then extended from a 1–D acoustooptic spectrum analyzer to a 2–D configuration for simultaneous spectrum analysis and direction–of–arrival determination. Two specific 2- D architectures are described and analyzed: a linear antenna array configuration and a novel circular antenna array with a Butler matrix beamformer configuration.

Emphasis is placed on the direction–finding characteristics of the two architectures. The effects of scaling factor, acoustic transducer height, Gaussian illumination profile, amplitude and phase tracking errors and RF input noise on the DOA pattern produced by each architecture are examined. Design criteria and example on each architecture are given. Finally the two architectures are compared.

2.0 FOURIER TRANSFORMING CONFIGURATION

A Fourier transforming configuration is shown in Fig. 2, where a Bragg cell in the object plane is illuminated with a monochromatic, collimated light wave. The incident light wave impinging on the object plane is given by

$$E(x,y,z,t) = E_o(x_o,y_o)\cos(2\pi\nu t - kz + \phi_o)$$

$$= \mathrm{Re}\{ E_o(x_o,y_o)\exp[-j(2\pi\nu t - kz + \phi_o)]\} \qquad (1)$$

where ν is the optical frequency with phase constant k,
ϕ_o is some initial phase of the wave at $t = z = 0$, and
$E_o(x_o,y_o)$ is the amplitude distribution, which is normally Gaussian, of the incident collimated optical wave.

Assuming the Fourier transform lens is ideal and using phasor quantities, the amplitude distribution in the back focal or Fourier plane is related to the object plane by the Fourier transform [10].

$$U_1(x_1,y_1,t) = \iint_{-\infty}^{\infty} \frac{E_o(x_o,y_o)}{j\lambda F} T(x_o,y_o,t)\exp[-j\frac{2\pi}{\lambda F}(x_o x_1 + y_o y_1)]\,dx_o dy_o$$

$$= K_1 \iint_{-\infty}^{\infty} E_o(x_o,y_o)\,T(x_o,y_o,t)\exp[-j2\pi(ux_o+vy_o)]\,dx_o dy_o \qquad (2)$$

where a constant phase factor has been dropped,

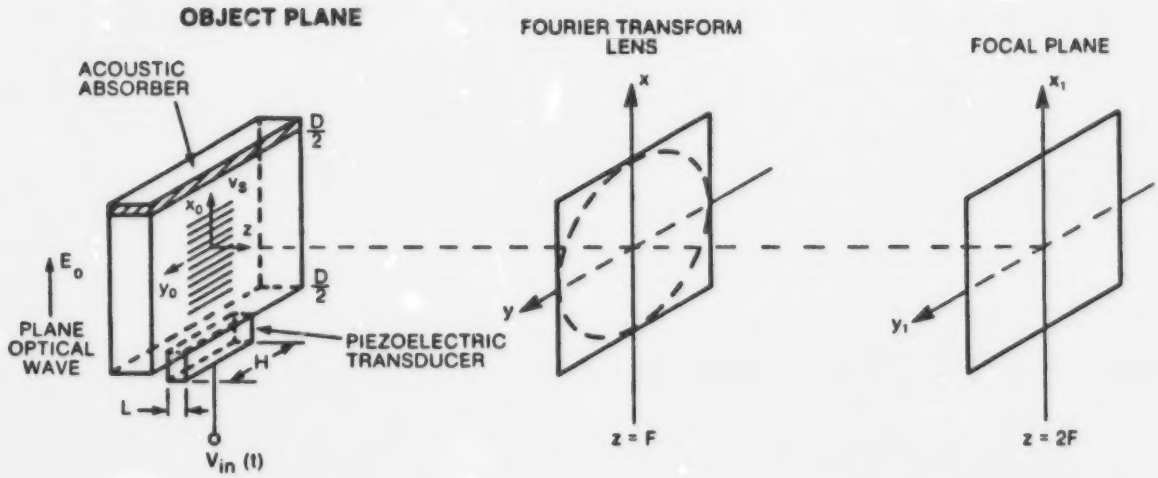

FIGURE 2: FOURIER TRANSFORMING CONFIGURATION

$$K_1 = \frac{1}{j\lambda F} \tag{3}$$

is a constant,

$$u = \frac{x}{\lambda F} \tag{4}$$

and $$v = \frac{y}{\lambda F} \tag{5}$$

are expressed in normalized coordinates, F is the focal length of the lens, λ is the optical wavelength and $T(x_o,y_o,t)$ is the complex transmission function of the Bragg cell which is now examined further in detail.

3.0 USE OF BRAGG CELLS AS SPATIAL LIGHT MODULATORS

An acoustooptic cell operating in the Bragg region is of particular interest as a spatial light modulator in an optical signal processor because only one strong diffraction order is generated[11–14].

Let the input signal to the modulator be expressed by a sinusoidal waveform

$$V_{in}(t) = A(t)\cos(2\pi f_s t + \phi_o) \tag{6}$$

where $A(t)$ is the amplitude function, f_s is the carrier frequency and ϕ_o is the initial phase of the signal. Let us assume that the acoustic beam profile is uniform in the y_o direction. For weak interactions, the normalized transmission function of the Bragg cell with only the higher first–order (up shift +1) component generated is approximately modeled by [15]

$$T(x_o,y_o,t) = \text{rect}\left(\frac{x_o}{D}\right)\text{rect}\left(\frac{y_o}{H}\right)\left\{1 + jK_B\, A\left(t - \frac{x_o}{v_s}\right)\right.$$

$$\left. \cdot \exp\left[-a\tau\left(\frac{x_o}{D} + \frac{1}{2}\right)\right]\exp\left[-j2\pi f_s\left(t - \frac{x_o}{v_s}\right)\right]\right\} \tag{7}$$

where

$$\text{rect}(x) = \left\{ \begin{array}{l} 1\,,\ |x| \leq 1/2 \\ 0, \text{otherwise} \end{array} \right\} \tag{8}$$

There are two terms in the transmission function; one is the zeroth order with a value of unity and the other term contains the signal information. This is given for the case where the diffracted order has the same polarization as the undiffracted (zeroth) order. If the acoustic wave is a shear wave, then a change in polarization by 90 degrees will also occur [16]. The acoustic signal is attenuated as it propagates across the aperture in the x direction with velocity v_s. The acoustic loss coefficient in Np/sec is denoted by a and is a function of frequency; τ is the acoustic transit time across the aperture D ,$A(t - x_o / v_s)$ is the complex amplitude function of the input signal, K_B is a constant which is proportional to the square root of the acoustooptic diffraction efficiency of the Bragg cell, K_B also takes into account the conversion efficiency of the piezoelectric transducer, and a constant phase term has been dropped.

For small input Bragg and diffraction angles, the amplitude distribution of the signal waveform is approximately given by substituting Eq.(7) into Eq.(2). Hence

$$U_1(u,v,t) = \frac{K_B}{\lambda F} \iint_{-\infty}^{\infty} g(t - \frac{x_o}{v_s})\, w(x_o,y_o)$$

$$\cdot \exp[-j2\pi(ux_o + vy_o)]\, dx_o\, dy_o \qquad (9)$$

$$\text{where} \quad g(t - \frac{x_o}{v_s}) = A(t - \frac{x_o}{v_s}) \exp[-j2\pi f_s (t - \frac{x_o}{v_s})] \qquad (10)$$

is the signal function . Again a constant phase term has been dropped.

$$w(x_o,y_o) = K\, \text{rect}(\frac{x_o}{D})\, \text{rect}(\frac{y_o}{H}) \exp[-(2Tx\frac{x_o}{D})^2 - (2Ty\frac{y_o}{H})^2]$$

$$\cdot \exp[-a\tau(\frac{x_o}{D} + \frac{1}{2})] \qquad (11)$$

is the amplitude weighting function. The incident light wave is assumed of Gaussian profile, with Tx and Ty specifying the Gaussian profile in the x_o and y_o dimensions respectively. K is the peak amplitude of the incident light wave.

Equation (9) simply states that the diffracted instantaneous amplitude distribution in the Fourier plane is the single–sided Fourier transform of the weighted input signal. A unique feature of this configuration is that the Fourier transform is computed over a sliding window of the input signal. At different time intervals, the Fourier transform of a different portion of the weighted signal is performed. When the acoustic diffraction effect in the y direction is neglected, the acoustooptic Fourier transformation is completely characterized by Eq.(9). In the case of a continuous wave (CW) signal of unity amplitude and for a rectangular weighting function, the amplitude distribution in the Fourier plane can be expressed in closed forms

$$U_1(u,v) = \frac{KK_B}{\lambda F} DH \exp(-j2\pi f_s t) \exp\left(j\frac{\pi D}{\lambda}\right) \mathrm{sinc}(vH)\, \mathrm{sinc}\left[D\left(u - \frac{f_s}{v_s}\right)\right] \tag{12}$$

where

$$\mathrm{sinc}(x) = \sin(\pi x)/(\pi x), \tag{13}$$

and λ is the acoustic wavelength. The amplitude distribution, parallel to the normalized u axis, is the single–sided Fourier transform of the truncated input signal .The distance from axis origin (u = 0) to the centroid of the distribution is linearly proportional to the acoustic frequency.

The analysis presented so far is for the case where the acoustic wave in the y direction is assumed to be uniform in amplitude and plane in its phase front. The Bragg cell in this case is modeled by an ideal traveling wave modulator. This is only true when a self–collimating acoustic beam is generated inside the Bragg cell crystal. It is also approximately true when the height (H) of the acoustic transducer is many orders larger than the acoustic wavelength in which the diffraction effect can be neglected. However in the latter case, there is usually a conflicting requirement in which H must be kept small. This is due to the fact that the diffraction efficiency [12,14] of a Bragg cell is directly proportional to the ratio of L/H ,where L is the width of the transducer. For broadband operation, L must be kept small to give an appreciable spread in the acoustic angular spectrum to satisfy the momentum conservation criterion. In order to maintain a large diffraction efficiency which is directly proportional to L/H, H must also be kept to a small value. Moreover, as will be discussed in Section 6, the height H must be kept small in a multi–channel Bragg cell configuration to preserve the diffraction pattern for DOA determination. Under these various circumstances and also depending on the characteristics of the Bragg cell crystal [17–20], the acoustic diffraction effect on the characteristics of the diffraction pattern can be appreciable and must be considered.

The acoustic diffraction effect on the output of a spectrum analyzer has been investigated by Vander Lugt [17] and other nonlinear effects have also been reported by others [18–20]. In order to keep the system analysis simple, the ideal traveling wave modulator model is used in this report. This simplified model is very useful for general system analysis such as in the development of processing architectures. The acoustic diffraction effect on the 2–D acoustooptic signal processors will be addressed in another report [21].

4.0 2–D ACOUSTOOPTIC FOURIER TRANSFORMING PROCESSORS

The basic 2–D acoustooptic configuration was first proposed by Lambert et al [5] to process radar echo signals received by the elements of a large phased array. The array structure considered was periodic with spacings less than half of the radar signal carrier wavelength. It was used for radar applications where the signal was known and the bandwidth of operation was narrow.

In Radar ESM receiver applications [1] the requirements are quite different, and a different set of design criteria has to be used. The key differences are that the frequency range of coverage is much broader and the number of parallel channels used must, for economic reasons, be kept small.

We now analyze two architectures: one using a linear antenna array and the other employing a circular antenna array with a Butler matrix beamformer. A mathematical expression is derived on the optical distribution as a function of the DOA and frequency of the received signal for these two processing architectures.

4.1 Processor Architecture Employing A Linear Antenna Array

In this section, a processor architecture employing a multi–channel Bragg cell fed with signals derived from a linear antenna array as shown in Fig. 3 is analyzed. The wavefront of the signal is assumed to be received in the azimuthal plane with the elevation angle equals to zero. If the elevation angle is not zero, the antenna element far–field pattern as a function of elevation angle has to be taken into account. In addition, a "Coning" angle error is also introduced [22–23].

For a CW or pulse–modulated carrier signal received from an emitter at an azimuthal angle θ ,the relative signal strength at the nth antenna is

$$V_n(t) = a_n(f_R,\theta)\, A(t-\tau_n')\cos[2\pi f_R(t-\tau_n') + \phi_o] \tag{14}$$

$$\text{where}\quad \tau_n' = \frac{d_n}{c}\sin(\theta) = \frac{d_n}{\lambda_R f_R}\sin(\theta), \quad n = 1,2,3,\ldots N \tag{15}$$

and $a_n(f_R,\theta)$ is the normalized antenna element far–field pattern, f_R is the RF frequency , λ_R is the RF signal wavelength, ϕ_o is the initial phase of the signal, $A(t-\tau_n')$ is the signal amplitude function, d_n is the distance measured from the array center to the nth antenna element. This distance is positive when located to the right of the array center and negative when on the left.

If the maximum delay τ_n' is much less than the duration of the signal, we can neglect the envelope delay, and the nth heterodyned IF signal is

$$V_{IF,n}(t) = A(t)\cos[2\pi(f_i t - \beta_n) + \phi_o]\, a_n(f_R,\theta) \tag{16}$$

$$\text{where}\quad \beta_n = \tau_n' f_R = \frac{d_n}{\lambda_R}\sin(\theta) \tag{17}$$

is the phase delay of channel n and f_i is the down–converted frequency and a unity gain is assumed for the RF to IF conversion.

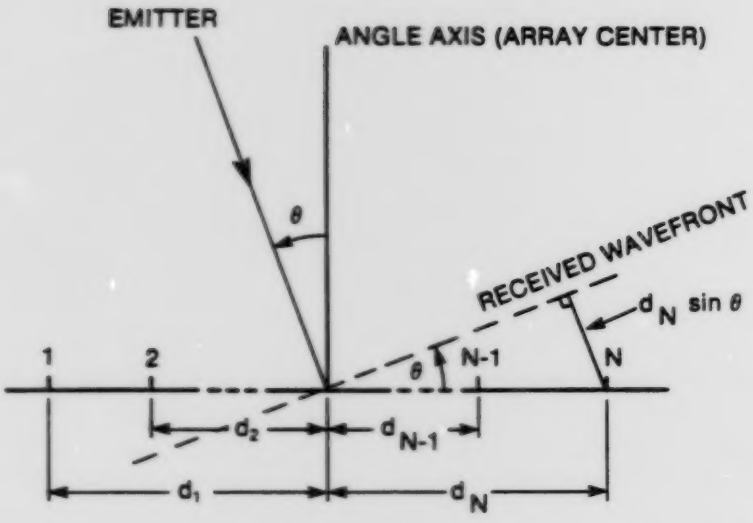

FIGURE 3: LINEAR ANTENNA ARRAY CONFIGURATION

The IF signal derived from each antenna element of frequency is fed into a multi–channel Bragg cell as shown in Fig. 4. In this architecture, the relative acoustic channel separation spacings are required to be the same as those of the microwave antenna spacings. This requirement is discussed further in Section 5.

In this report, the ideal traveling wave modulator model is used and thus the acoustic beam can simply be represented by rectangular functions. Moreover, the cross–talks among the channels are assumed to be negligible. For N identical channels, the complex transmission function of the multi–channel Bragg cell is obtained by substituting Eq.(16) into Eq.(7). Hence

$$T(x_o,y_o,t) = \sum_{n=1}^{N} \text{rect}(\frac{x_o}{D}) \text{rect}(\frac{y_o - \ell_n}{H}) \cdot \Big[1 + jK_B A(t - \frac{x_o}{v_s}) \exp[-a\tau(\frac{x_o}{D} + \frac{1}{2})] a_n(f_R,\theta) \cdot \exp\{-j[2\pi f_i(t - \frac{x_o}{v_s}) - 2\pi\beta_n + \phi_o]\}\Big] \quad (18)$$

The multi–channel Bragg cell is used in the same Fourier transforming configuration as described in Section 2. A collimated laser source is used to illuminate the multi–channel Bragg cell at the Bragg input angle. A 2–D Fourier transform is carried out by using a spherical Fourier transform lens with a focal length F. The amplitude distribution in the Fourier plane is obtained by substituting Eq.(18) into Eq.(2). Making use of the shifting property of the Fourier transform pair in the y_o dimension and after some grouping of terms, the diffracted order which contains the signal information becomes

$$U_1(u,v,t) = K_2 f(v) \iint_{-\infty}^{\infty} g(t - \frac{x_o}{v_s}) w(x_o,y_o) \exp[-j2\pi(ux_o + vy_o)] dx_o dy_o \quad (19)$$

where $$K_2 = \frac{NK_B}{\lambda F} \exp(-j\phi_o) \quad (20)$$

and

$$f(v) = \frac{1}{N} \sum_{n=1}^{N} a_n(f_R,\theta) \exp[-j2\pi(v\ell_n - \beta_n)] \quad (21)$$

is the normalized complex DOA pattern of the optical array, ℓ_n is the distance measured from the center of the acoustic transducer array to the nth transducer element , a_n is the

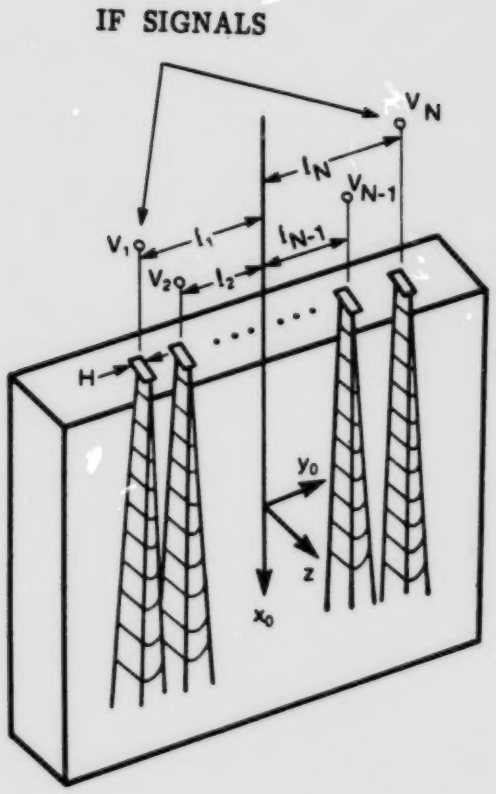

FIGURE 4: MULTI–CHANNEL BRAGG CELL CONFIGURATION

normalized amplitude weighting of the diffracted light beam appearing in the nth channel, and

$$w(x_o,y_o) = K\ \mathrm{rect}(\frac{x_o}{D})\ \mathrm{rect}(\frac{y_o}{2\ell_N})\ \exp[-(2Tx\frac{x_o}{D})^2 - (2Ty\frac{y_o}{2\ell_N})^2]$$

$$\cdot\ \exp\ [-a\tau\ (\frac{x_o}{D} + \frac{1}{2})] \qquad (22)$$

is the window weighting function for Gaussian interaction profile. Tx and Ty specify the Gaussian profile in the x_o and y_o dimensions respectively. $2\ell_N$ is the length of the acoustic transducer array. The optical distribution, characterizing the frequency and DOA information along the u and v coordinates respectively, has thus been derived.

4.2 Processor Architecture Using A Circular Antenna Array And A Butler Matrix

The linear antenna array coupled to a multi–channel Bragg cell, has a limited instantaneous angular field–of–view. It is usually less than 180 degrees in azimuth and typically a 90 degree field–of–view is obtained. In order to increase the instantaneous field–of–view to 360 degrees, another novel architecture using a circular antenna array is needed. In this architecture a Butler matrix beamformer is used to couple the outputs from the circular antenna array to a multi–channel Bragg cell. A typical implementation of the antenna structure with a Butler matrix is shown in Fig.5 [24]. The Butler matrix is essentially a phase shifting network containing 180–degree hybrids, 90–degree hybrids and phase shifters. It is a passive device having N inputs and N outputs where N is usually a power of 2. All inputs are isolated from one another and a signal applied at the output port will result in equal amplitudes at all antenna elements but with the relative phase of each antenna varying linearly across the array [25]. Specifically, if N is even and the nth input port is energized $n = 0, \pm1, \pm2, \ldots, \pm(N-2)/2, \pm N/2$, the difference in phase between adjacent ports is $2\pi n/N$ and the total phase variation around a circular array connected to the Butler matrix would be $2\pi n$, which is the nth mode. Not all the output ports are used in this application and the purpose is not to form a narrow beam in the azimuth plane, but to get omnidirectional coverage. Power applied to output port n of the feed network generates modes at the antenna array with an $\exp(jn\theta)$ phase progression, where θ is the bearing angle and n is the mode number related to each output port. For N antenna elements the following modes are possible: $n = 0, \pm 1, \pm 2, \pm 3, \ldots, \pm (N/2 - 1), \pm N/2$. In the far field of the array the pattern is omnidirectional in azimuth for all modes. The ideal phase variation versus bearing angle is shown in Fig. 6 for modes $n = +1, +2$ and -2. In general, the ideal phase variation versus bearing angle θ for mode n equals $n\ \theta$.

If a signal source is located at an azimuthal angle θ, and from reciprocity, the received phase at the $n = +1, +2$ and -2 output ports of the feed network will have the same relationship as the far field phase in the transmit mode. A phase comparison of the $n = +2$ and $n = +1$ output ports is a direct measurement of the bearing angle . Note that the measured phase equals the bearing angle independent of frequency.

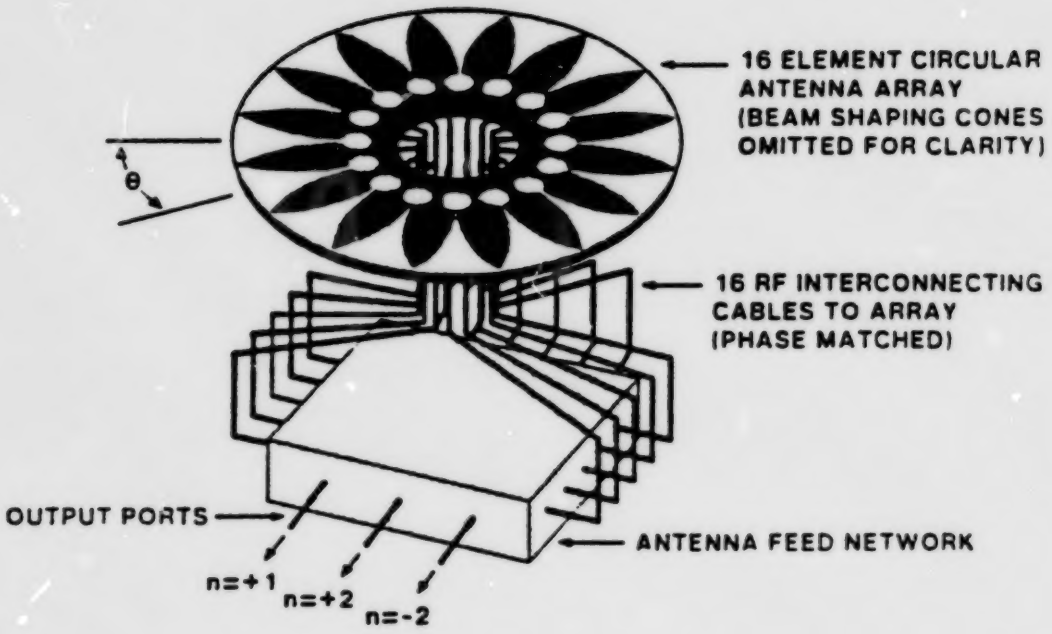

FIGURE 5: CIRCULAR ANTENNA ARRAY AND FEED NETWORK

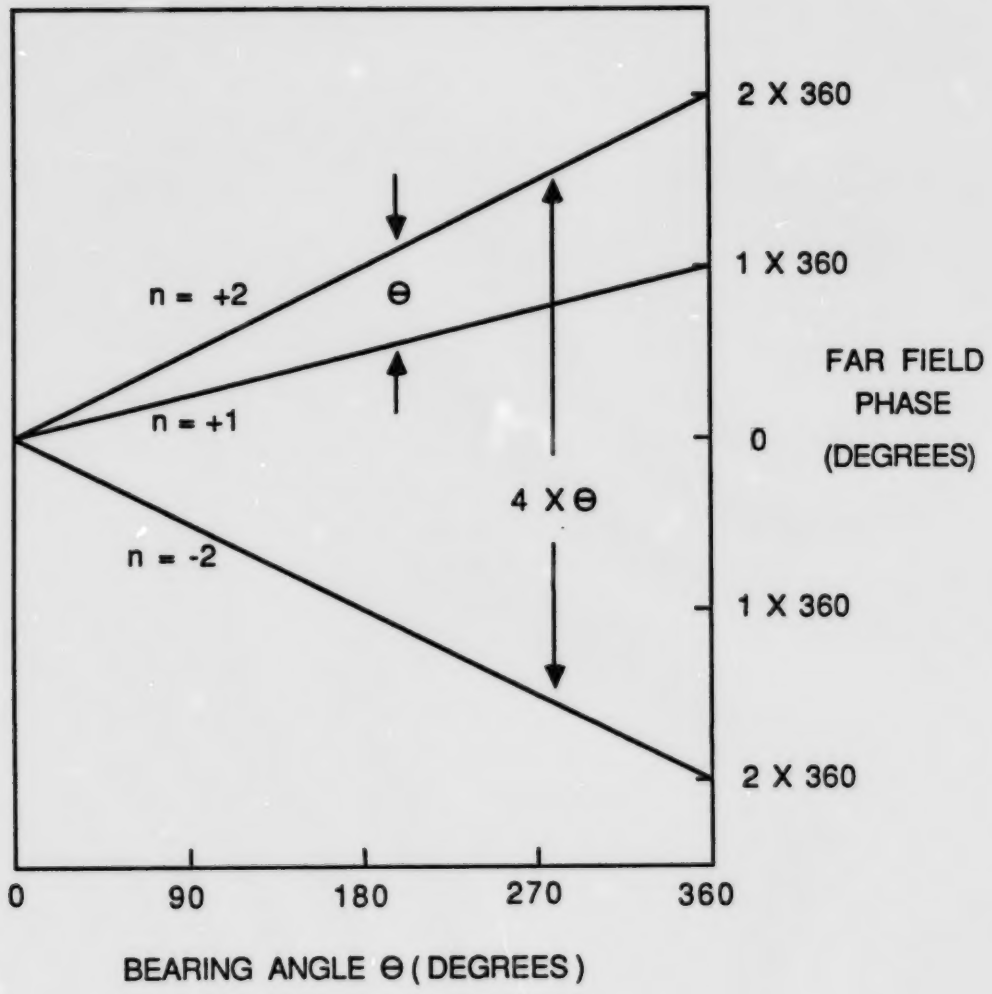

FIGURE 6: PHASE IN THE FAR FIELD VERSUS BEARING ANGLE

Following a similar down–conversion process as in the linear antenna array architecture, the signals from the output ports of the Butler matrix are first down–converted to a lower intermediate frequency and then applied to the transducers of a multi–channel Bragg cell. Since the phase variation from port n equals n θ, a periodic multi–channel Bragg cell structure is needed. The nth heterodyned IF signal is

$$V_{IF,n}(t) = A(t) \cos[2\pi (f_i t - \beta_n) + \phi_o] \, a_n(f_R) \tag{23}$$

where $a_n(f_R)$ is now the normalized gain of the circular antenna array with the Butler matrix beamformer. It is assumed to be ideal and independent of azimuth, and

$$\beta_n = n (\theta - \theta_{os}) \tag{24}$$

With the bearing offset (θ_{os}) adjusted to zero, an ideal phase relationship is obtained from output port n. In this case when a signal is received at $\theta = 0$, all the phase angles (β) are zero. If the bearing offset is not zero, then a fixed linear phase shift ($n\theta_{os}$) will be introduced across the array. This will only shift the diffracted optical beam and thus will result in an offset in the measured bearing.

A typical architecture, using a 32–element circular array and a Butler matrix with 9 output ports of n = 0 , ±1 ,± 2, ± 3, ± 4, is shown in Fig. 7.

A similar analysis as given in Section 4.1 can be carried out for this architecture. The diffracted order which contains the signal information is again given by the general expressions in Eqs.(19) to (22).

5.0 SCALING FACTOR (S.F.)

The main lobe of the DOA pattern is obtained by setting the exponent of Eq.(21) to zero and thus

$$v = \beta_n / \ell_n \quad , \quad \text{for } n = 1,2,...N \tag{25}$$

For the linear antenna array configuration, the main lobe location is related to the DOA (θ) of the received signal by substituting β from Eq.(17) to yield

$$v = \frac{d_n}{\lambda_R \ell_n} \sin(\theta) \tag{26}$$

and making use of Eq.(5)

$$y_1 = \frac{\lambda \, d_n}{\lambda_R \ell_n} F \sin(\theta) \tag{27}$$

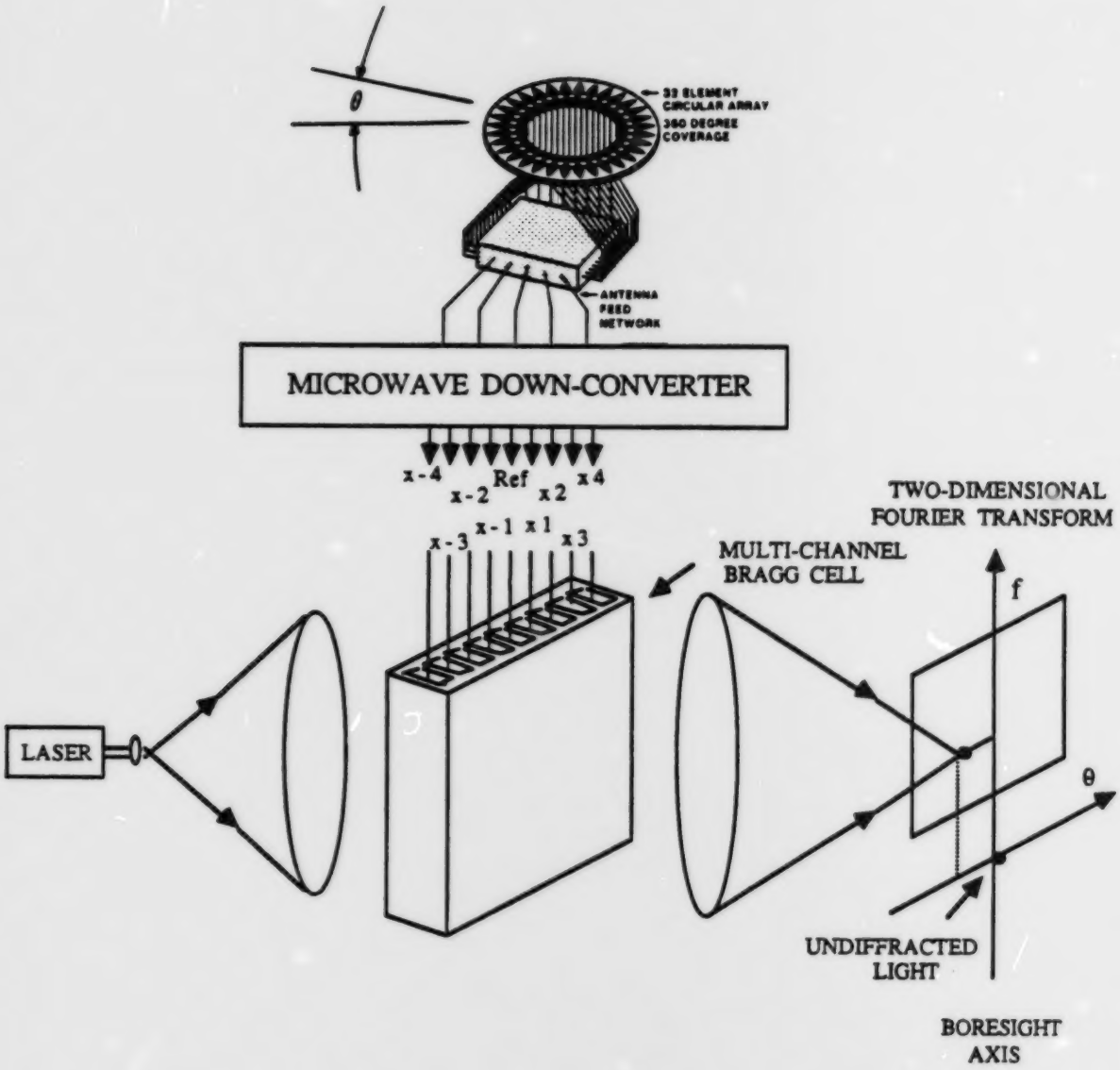

FIGURE 7: TWO–DIMENSIONAL ACOUSTOOPTIC RECEIVER USING A CIRCULAR ANTENNA ARRAY AND A BUTLER MATRIX

where the ratio of the antenna element spacing to the acoustic transducer spacing (d_n/ℓ_n) is chosen to be a constant in this architecture . As a result, the optical array pattern produced will be a close replica of the antenna array pattern. The location of the main lobe (y_1), is proportional to $\sin(\theta)$. Let us define the ratio of the antenna array length in wavelengths to the optical array length in wavelengths by a scaling factor (S.F.). That is

$$S.F. = (d_n/\lambda_R)/(\ell_n/\lambda) \tag{28}$$

Making use of Eq.(27), the scaling factor can also be related to the main lobe location and the DOA (θ) of the signal by

$$S.F = y_1/\,[F \sin(\theta)] \tag{29}$$

The optical frequency of the diffracted beam is actually doppler shifted by an amount equal to the acoustic signal frequency. However in most practical cases, the doppler shifts introduced are very small in comparison to the optical carrier frequency and thus the scaling factor can be assumed to be directly proportional to the input RF signal frequency only. The scaling factor is normally much less than unity and therefore the deflection angle (ϕ) of the main lobe is given by

$$\phi = \tan^{-1}(y_1/\,F) \approx y_1/\,F \quad , \text{ for } y_1/\,F << 1 \tag{30}$$

and making use of Eq.(28), yields

$$\phi = S.F.\ \sin(\theta) \tag{31}$$

$$\approx S.F.\ \theta \quad , \text{for } \theta << 1 \tag{32}$$

For the circular antenna array configuration, the effective normalized antenna array length is N and thus the scaling factor is

$$S.F. = N\lambda/(N\ell) = \lambda/\ell \tag{33}$$

which is independent of the input signal frequency and ℓ is the smallest transducer element–to–element spacing. Substituting v from Eq.(5) and β_n from Eq.(24) into Eq.(25), and making use of Eq.(33), the scaling factor can also be expressed by

$$S.F = y_1/\,(F\ \theta) \tag{34}$$

Substituting Eq.(34) into Eq.(30), the optical deflection angle (ϕ) of the main lobe is

$$\phi \approx S.F.\ \theta \tag{35}$$

Equations (31) and Eq.(35) simply state that the optical array steering angle is scaled down from the microwave antenna array steering angle by the scaling factor (S.F.). Once the location of the main lobe is determined in the Fourier plane, the DOA of the

emitter for the linear antenna array configuration is given by

$$\theta = \sin^{-1}\left(\frac{y_1}{F \cdot S.F.}\right), \tag{36}$$

and for the circular antenna configuration, by

$$\theta = \frac{y_1}{F \cdot S.F.} \tag{37}$$

6.0 EFFECT OF TRANSDUCER HEIGHT ON DOA PATTERN

For a continuous wave or pulse–modulated CW filling up the multi–channel Bragg cell aperture, and with a rectangular window weighting

$$w(x_o,y_o) = \text{rect}\left(\frac{x_o}{D}\right) \text{rect}\left(\frac{y_o}{H}\right), \tag{38}$$

the instantaneous diffracted light distribution as given in Eq.(19) can be simplified to

$$U_1(u,v,t) = \frac{K_B DH}{\lambda F} \exp[-j2\pi f_i(t+\phi_o)] \, \text{sinc}[D(u - \frac{1}{\lambda})]$$

$$\cdot \, \text{sinc}(vH) \sum_{n=1}^{N} a_n(f_R,\theta) \exp[-j2\pi (v\ell_n - \beta_n)] \tag{39}$$

The DOA information is completely contained in the optical array pattern term. Its shape must be preserved in order to determine the peak main lobe location. This is critical in the case of an aperiodic array configuration with a few elements, in which the sidelobe levels are usually only a few dB below the main lobe. The main lobe can be detected only if the weighting function [sinc(vH)] is kept relatively constant and varies smoothly over all values of v of interest. In order to satisfy this condition, H must be kept small.

An example is used to illustrate the requirement of H for the linear antenna array processor configuration. For a certain scan angular range $\Delta\theta$, the corresponding range of v is given by Eq.(26). If the sinc (vH) function is required to vary by less than 10% from its maximum value of unity within the scan angle (θ) of ±90 degrees, the corresponding v is

$$v = \frac{d_n}{\lambda_R \ell_n} \sin(\theta), \quad \theta = \pm 90^\circ \tag{40}$$

Substituting the range of v into sinc(vH), the following condition must be met

$$\text{sinc}(vH) = \frac{\sin[\pi(\frac{d_n H}{\lambda_R \ell_n})]}{\pi \frac{d_n H}{\lambda_R \ell_n}} \geq 0.9 \qquad (41)$$

Hence $$H \leq \frac{\ell_n \lambda_R}{4\, d_n} \qquad (42)$$

In practical systems, the amplitude window weighting function is given by Eq. (22). The function is assumed to be of truncated Gaussian distributions in both the x and y dimensions. The general effect of the truncated Gaussian laser profile and acoustic attenuation on both the instantan/ous and time–integrated waveform distributions from an acoustooptic spectrum analyzer are well known [4],[26]. The general effect of the weighting function is to broaden the main lobe of the sinc function while the sidelobe levels are suppressed. As a result, the condition stated by Eq.(42) can be relaxed somewhat due to this broadening effect.

7.0 GAUSSIAN LASER ILLUMINATION PROFILE

Laser beam profile of Gaussian distribution is important in optical signal processing because the intensity profile of most gas lasers such as HeNe is characterized by the Gaussian distribution [27]. In addition, the intensity profile of the lowest order beam from a double heterostructure solid state laser is also of Gaussian shape. The Gaussian profile can be modified (expanded or reduced) easily in one or two dimensions by using a beam–expander such as an anamorphic prism beam–expander [28–29]. In this section, the effect of the Gaussian illumination profile on the DOA pattern is investigated.

When a multi–channel Bragg cell is illuminated "fully" in the y_o dimension with a Gaussian laser beam, the amplitude weighting function as given by Eq.(22) is modified to give

$$\begin{aligned} w(x_o,y_o) &= w(x_o)\, w(y_o) \\ &= \left[\sqrt[4]{2/\pi}\, \sqrt{2Tx/D}\ \text{rect}(\frac{x_o}{D}) \exp[-(2Tx\frac{x_o}{D})^2] \exp\left[-a\tau\,(\frac{x_o}{D} + \frac{1}{2})\right]\right] \\ &\quad \cdot \left[\sqrt[4]{2/\pi}\, \sqrt{Ty/\ell_N}\ \exp[-(2Ty\frac{y_o}{2\ell_N})^2]\right] \\ &= \left\{ \sqrt[4]{2/\pi}\, \sqrt{2Tx/D}\ \text{rect}(\frac{x_o}{D})\ \exp\left[\frac{a\tau}{2}[\frac{a\tau}{8Tx^2} - 1]\right]\right. \\ &\quad \left. \cdot \exp\left[-[2Tx\,(\frac{x_o}{D} + \frac{a\tau}{8Tx^2})]^2\right]\right\} \left\{ \sqrt[4]{2/\pi}\, \sqrt{Ty/\ell_N}\ \exp[-(2Ty\frac{y_o}{2\ell_N})^2]\right\} \qquad (43) \end{aligned}$$

The total intensity of the incident laser beam has been normalized to a maximum value of unity when the acoustic loss factor is zero . In this normalized form the total intensity will remain constant independent of the values of the Gaussian profile parameters. We first calculate the amplitude distribution in the Fourier plane in the case where the amplitude weighting function is of a rectangular distribution. The Gaussian and acoustic exponential functions are then accounted for by convolving the amplitude distribution with the Fourier transform of Eq.(43). The Fourier transform of the normalized weighting function can be separated into two independent functions of u or v only. That is

$$W(u,v) = W(u)\, W(v) \tag{44}$$

$$\text{where } W(u) = \int_{-\infty}^{\infty} w(x_o) \exp(-j2\pi u x_o)\, dx_o \tag{45}$$

$$\text{and } W(v) = \int_{-\infty}^{\infty} w(y_o) \exp(-j2\pi v y_o)\, dy_o$$

$$= \sqrt[4]{2/\pi}\, \sqrt{\pi \ell_N / Ty}\, \exp[-(\pi v \frac{\ell_N}{Ty})^2] \tag{46}$$

is again of Gaussian distribution. The amplitude distribution in the Fourier plane is obtained by convolving Eq. (44) with Eq.(39) to yield

$$U_i(u,v,t) = \left[\frac{K_B DH}{\lambda F} \exp[-j2\pi f_i(t+\phi_o)]\, \text{sinc}[D(u - \frac{1}{\lambda})]\, \text{sinc}(vH) \right.$$

$$\left. \cdot \sum_{n=1}^{N} a_n(f_R, \theta) \exp[-j2\pi (v\ell_n - \beta_n)] \right]$$

$$* \left[W(u) \sqrt[4]{2/\pi}\, \sqrt{\pi \ell_N / Ty}\, \exp[-(\pi v \frac{\ell_N}{Ty})^2] \right] \tag{47}$$

where * denotes convolution. We are mainly interested in determining the effect of the Gaussian input laser profile $w(y_o)$ on the DOA pattern and thus from the above equation, only the W(v) component is of interest. It is expected that if the acoustic beam width, including the acoustic spreading in the y dimension, is much smaller than the Gaussian illumination beam width, the Gaussian weighting on each acoustic beam can be assumed to be approximately uniform. In this case, the convolution given in Eq. (47) in the v dimension can be simplified by performing it in the (x_o, y_o) domain. This is done by just multiplying the amplitude of each acoustic channel by the Gaussian weighting $w(y_o)$ located at the channel center. In other words, each acoustic beam can be approximated by a self–collimating beam with height H and illuminated with uniform intensity.

7.1 DOA Main Lobe Intensity Versus Gaussian Profile Parameter Ty

The input Gaussian illumination profile has been chosen to be located symmetrically with respect to the acoustic array center. This is due to the reason that a displaced Gaussian function can be expressed in terms of a product of a centrally located Gaussian function of the same distribution and an exponential function as given in Eq.(43). The exponential function has the undesirable effect of increasing the sidelobe levels in the Fourier plane [26].

The intensity distribution of the DOA pattern as a function of the input Gaussian illumination profile parameter Ty is investigated in Sections 11.2 and 12.0. For a fixed total laser power interacting with the acoustic beams, it can be shown that the intensity of the main lobe of the DOA pattern will reach a maximum when all the channels are of equal amplitude. For Gaussian illumination profile, the total interacting optical power and its resultant output intensity of the DOA pattern are only a function of the Gaussian profile parameter Ty. A maximum in the total optical power interacting with the acoustic beams usually may not result in a maximum main lobe intensity on the DOA pattern.

For the linear antenna array configuration, the DOA pattern is a function of the specific channel locations and is illustrated later in Section 11.2 by using an optimum 4–element array. For the circular antenna array configuration it is a function of whether the array is odd or even and whether the array is filled or not. The effect of the Gaussian illumination profile parameter Ty on the DOA pattern is analyzed further in Section 12.

8.0 ERROR TOLERANCE ANALYSIS

An incoming electromagnetic wave front is sampled spatially by the antenna array. The signal received by each antenna element is then separately down–converted and amplified by various active and passive components. It is then finally converted into a traveling acoustic wave by the piezoelectric transducer. The resulting acoustic columns interact with the collimated laser beam, producing the desired diffracted wavefront.

A large number of occurrences can cause the actual optical array pattern to be far from the ideal predicted by the assumed deterministic models. Since most components are amplitude and phase sensitive to variations in frequency, then the signal passing through each channel experiences phase and amplitude errors. Phase errors are also introduced by errors in the placement of antenna elements and acoustic transducers. Mutual coupling can also be a major phenomenon affecting both amplitude and phase in both arrays. In addition, the optical system also introduces aberrations which affect both the phase and amplitude of the optical wavefront.

Irrespective of which phenomenon is responsible for an error, the only effect it may have is on the amplitudes and the phases of the signals. Hence any error source may be typified by error δa_n and $\delta \phi_n$ to the amplitude and phase of the nth channel, respectively.

8.1 Optical Array Pattern

Introducing the amplitude and phase errors into Eq. (21), the normalized optical array pattern can be written as

$$f(v) = \frac{1}{N} \sum_{n=1}^{N} (a_n + \delta a_n) \exp(j\delta\phi_n) \exp[-j2\pi (v\ell_n - \beta_n)], \tag{48}$$

where the dependent variables have been dropped for clarity. The expected value of the intensity pattern is

$$E[f(v)f^*(v)] = \frac{1}{N^2} E \left[\sum_{n=1}^{N} \sum_{m=1}^{N} (a_n + \delta a_n)(a_m + \delta a_m) \right.$$

$$\left. \cdot \exp[j(\delta\phi_n - \delta\phi_m)] \exp\{-j2\pi[v(\ell_n - \ell_m) - (\beta_n - \beta_m)]\} \right] \tag{49}$$

where * denotes complex conjugate.

In the following analysis, the means of the amplitude and the phase errors are assumed to be zero. All errors are independent of each other and the nth amplitude error is independent of the nth amplitude.

Following a similar analysis as given by Steinberg [30], the expected intensity pattern for the array can be shown to be

$$E[f(v)f^*(v)] = \left|\overline{\exp(j\delta\phi)}\right|^2 f_o(v) f_o^*(v) + \frac{1}{N^2}\left[1 - \left|\overline{\exp(j\delta\phi)}\right|^2 \right] \sum_{n=1}^{N} a_n^2$$

$$+ \frac{1}{N^2} \sum_{n=1}^{N} \sigma_{a_n}^2 \tag{50}$$

If the amplitudes are of equal weighting of value a and variance σ_a^2, then

$$E[f(v)f^*(v)] = \left|\overline{\exp(j\delta\phi)}\right|^2 f_o(v) f_o^*(v) + a^2\left[\left[1 - \left|\overline{\exp(j\delta\phi)}\right|^2 + \sigma_a^2 \right] / N \right. \tag{51}$$

where $f_o(v)$ is the designed pattern with no errors.

If the phase error has a normal power spectral distribution function with variance σ_ϕ^2, then

$$\left|\overline{\exp(j\delta\phi)}\right|^2 = \left| E[\exp(j\delta\phi)] \right|^2$$

$$= \left| \int_{-\infty}^{\infty} \exp(j\delta\phi) \frac{\exp[-\delta\phi^2/(2\sigma_\phi^2)]}{\sqrt{2\pi}\ \sigma_\phi} d\delta\phi \right|^2$$

$$= \exp(-\sigma_\phi^2) \tag{52}$$

All the directional properties are in the first term of Eq. (51) and are unchanged from the intensity pattern of the error–free array. The remainder is an angle–independent contribution to the expected pattern, and its magnitude is inversely proportional to the number of channels. The dominant effect is a reduction in gain and a change in the main lobe to sidelobe ratios.

8.2 RMS Beam–Pointing Error

The amplitude errors alone produce no pointing errors. Hence only the effect of phase errors is analyzed.

The assumed statistics are

$$E(\delta\phi_n) = E(\delta\phi_m) = 0, \qquad \text{all } n,m \tag{53}$$

$$E(\delta\phi_n \delta\phi_m) = 0, \qquad n \neq m, \tag{54}$$

and

$$\sigma_\phi^2 = E(\delta\phi^2) << 1 \tag{55}$$

Let $\delta\phi_n - \delta\phi_m = \delta\phi_{nm}$, $\ell_n - \ell_m = \ell_{nm}$ and $\beta_n - \beta_m = \beta_{nm}$, the intensity pattern as given by Eq.(48) can be rewritten as

$$f(v)f^*(v) = \frac{1}{N^2} \sum_{n=1}^{N} \sum_{m=1}^{N} a_n a_m \exp[-j(2\pi v \ell_{nm} - \delta\phi_{nm} - 2\pi\beta_{nm})] \tag{56}$$

The pointing direction is found by setting the derivative of the above equation with respect to the variable v to zero. Assuming the pointing error is small and follow a similar analysis as given by Steinberg [30], the normalized optical RMS beam–pointing error as derived in Appendix A is

$$\sigma_{v_1} = \sigma_\phi \left[\left[\sum_{n=1}^{N} a_n \right]^2 \sum_{n=1}^{N} a_n^2 \ell_n^2 - 2 \sum_{m=1}^{N} a_m \sum_{n=1}^{N} \sum_{p=1}^{N} a_n^2 a_p \ell_n \ell_p \right.$$

$$\left. + \sum_{n=1}^{N} a_n^2 \sum_{m=1}^{N} \sum_{p=1}^{N} a_m a_p \ell_m \ell_p \right]^{1/2} / \left[\pi \sum_{n=1}^{N} \sum_{m=1}^{N} a_n a_m \ell_{nm}^2 \right] \tag{57}$$

where $v_1 = v - v_o$ (58)

and v_o is the normalized position of the steered diffracted optical beam with no pointing errors. Equation(57) is a general solution which takes into account the element weighting as well as the arbitrary locations of the elements. If the element locations are measured from the array center and the number of elements is greater than three, the last two terms in the numerator are negligible. The beam–pointing error is then approximated by

$$\sigma_{v_1} = \frac{\sigma_\phi \left[\left[\sum_{n=1}^{N} a_n \right]^2 \sum_{n=1}^{N} a_n^2 \ell_n^2 \right]^{1/2}}{\pi \sum_{n=1}^{N} \sum_{m=1}^{N} a_n a_m \ell_{nm}^2}$$

$$= \frac{\sigma_\phi \sum_{n=1}^{N} a_n \left[\sum_{n=1}^{N} a_n^2 \ell_n^2 \right]^{1/2}}{2\pi \left[\sum_{n=1}^{N} a_n \sum_{n=1}^{N} a_n \ell_n^2 - \left[\sum_{n=1}^{N} a_n \ell_n \right]^2 \right]} \qquad (59)$$

The beam–pointing error is directly proportional to the RMS phase error and inversely proportional to the array length ($2\ell_N$). It is also a function of the specific spatial distribution of the weighted channels. For N large, it can be shown that it is approximately inversely proportional to the square root of N[30]. If the amplitudes are of even symmetry about the center while the element positions are of odd symmetry, Eq.(59) can be simplified further to

$$\sigma_{v_1} = \frac{\sigma_\phi \left[\sum_{n=1}^{N} a_n^2 \ell_n^2 \right]^{1/2}}{2\pi \sum_{n=1}^{N} a_n \ell_n^2} \qquad (60)$$

The pointing error as given by Eqs.(57–59) can also be expressed in radians by making use of Eq.(5). Hence

$$\sigma_{y_1} / F = \sigma_{v_1} \lambda \qquad (61)$$

The pointing error, of the diffracted optical beam steered to v_o, has been expressed in terms of the normalized variable v in the Fourier plane. The pointing error expressed directly in terms of the DOA (θ) of the received signal is also of interest.

For the circular antenna array configuration, substituting v_o from Eq.(a5) into Eq.(a6) in Appendix A and making use of Eq.(24) with $\theta_{os} = 0$, we have

$$\begin{aligned} v_1 &= v - v_o \\ &= n\theta/\ell_n - (n-m)\theta_o/(\ell_n - \ell_m) \\ &= n\theta/\ell_n - (n-m)\theta_o/\,[(n-m)\ell] \\ &= (\theta - \theta_o)/\ell \end{aligned} \tag{62}$$

where θ_o is the DOA of the received signal with no pointing errors. As can be seen from the above equation, $(\theta - \theta_o)$ and $(v - v_o)$ are linearly related by the smallest transducer inter–element spacing ℓ.

For the linear antenna array configuration, the relationship between the two variables is more complex. Following a similar procedure and by making use of Eq.(17), we have

$$\begin{aligned} v_1 &= v - v_o \\ &= \frac{d_n}{\lambda_R \ell_n} \sin(\theta) - \sin(\theta_o)[(d_n/\lambda_R - d_m/\lambda_R)/(\ell_n - \ell_m)] \\ &= \frac{d_n}{\lambda_R \ell_n}[\sin(\theta) - \sin(\theta_o)] \end{aligned} \tag{63}$$

Expressing in terms of $(\theta - \theta_o)$ and $(v - v_o)$

$$\theta - \theta_o = \sin^{-1}[(v - v_o)\lambda_R \ell_n/d_n + \sin(\theta_o)] - \theta_o \tag{64}$$

Taking a partial derivative with respect to $(v - v_o)$

$$\frac{\partial(\theta - \theta_o)}{\partial(v - v_o)} = \frac{\lambda_R \ell_n/d_n}{\sqrt{1 - [(v - v_o)\ \lambda_R \ell_n/d_n + \sin(\theta_o)]^2}} \tag{65}$$

As a result, for small deviations $(\theta - \theta_o << 1)$ around the incoming bearing (θ_o), the above relationship can be simplified further

$$\Delta(\theta - \theta_o) \approx \frac{\lambda_R \ell_n/d_n}{\cos(\theta_o)} \Delta(v - v_o) \tag{66}$$

$$\text{for } |\sin(\theta_o)| >> |\,(v - v_o)\lambda_R \ell_n / d_n\,|,$$

where the measured bearing error $(\theta - \theta_o)$ due to phase errors is now inversely proportional to the cosine of the incoming bearing (θ_o), and

$$\Delta(\theta - \theta_o) \approx \lambda_R \ell_n / d_n \, \Delta(v - v_o) \tag{67}$$

$$\text{for } |\sin(\theta_o)| << 1$$

A relationship between the deviation in the normalized DOA pattern coordinate $(v - v_o)$ and the deviation of the measured bearing $(\theta - \theta_o)$ for the two configurations have been established by Eq.(62) and Eqs.(66) and (67). By substituting $(v - v_o)$ back into Eq.(a11), the pointing error can then be expressed directly in terms of $(\theta - \theta_o)$ and only a multiplication factor is needed.

9.0 EFFECT OF NOISE ON DETECTED DOA PATTERN

The RF signal to the 2–D acoustooptic signal processor is first amplified and then down–converted to an intermediate frequency (IF), f_s. The IF signal is applied to the transducer of a Bragg cell where it is converted to an acoustic signal. The acoustic signals in the various channels of the multi–channel Bragg cell are coherently illuminated with a laser beam. Through the process of acoustooptic interaction, a portion of the incident laser beam is diffracted by the signals. The Fourier transform is computed over a sliding window of the weighted input signal. The transformed signal appears as a light intensity distribution in the Fourier plane of the Fourier transform lens. This light intensity distribution, which is the magnitude squared of the 2–D Fourier transform of the signals in the multi–channel Bragg cell, is detected by a time–integrating 2–D photodetector array. At different instances in time, the Fourier transform of a different portion of the weighted signal is performed giving rise to the instantaneous DOA pattern along the y_1 axis and its instantaneous frequency spectrum along the x_1 axis. As the signal passes through the Bragg cell aperture, the instantaneous power spectra and the DOA patterns generated, are continuously integrated by the photodetector array. The time–integrated charge packets at discrete photodetector elements are then multiplexed to produce a sampled data waveform of the 2–D image.

So far, the optical diffraction pattern appearing on the Fourier plane has been analyzed with the effect of input noise neglected. The optical diffraction pattern is detected and converted back to electronic signal distribution by the use of a photodetector array. The input noise contribution of the 2–D acoustooptic signal processor is usually dominated by the RF front–end pre–amplifier noise since subsequent stages in the receiver are preceded by sufficient gain in order to overcome additional noise. As a result, the input noise can be assumed to be white Gaussian with spectral density $\eta/2$. After detection by the photodetector array, there is additional noise introduced by the photo detection process such as shot noise generated by the signal and detector dark current, thermal noise and

other detector noise sources [33]. The resultant signal–to–noise ratio of the sampled signal is also affected by the type of input signal, the integration time of the photodetector array and the pixel size.

The purpose of this 2–D processor is to provide power spectral density estimates and DOA information of radar signals. The use of a time–integrated photodetector array for detection reduces the amount of data generated from such a processor. Silicon CCD (charge coupled device) scanned solid–state 2–D photodetector arrays that are available commercially for TV applications feature integration times on the order of milliseconds [31–32]. However the use of such photodetector arrays does not provide accurate TOA (time of arrival) information on the radar signal, and other means such as using an additional acoustooptic spectrum analyzer with fast read–out times on the order of a microsecond must be considered. Photodetector array technologies having fast read–out times have been developed[33–36]. Another advantage of using an integrating photodetector array with long integration time is the increased sensitivity which may be achieved through the non–coherent integration produced by the time–integrating array [37–38].

For a CW signal, the TOA parameter is not relevant. A general statistical analysis on the noncoherent processing gain of an acoustooptic spectrum analyzer for various types of noise statistics as a function of the integration period, has been given for the case of a CW signal [37]. In addition, the degradation in signal sensitivity due to noise arising from the photo detection process, and the trade–off between noncoherent processing gain versus dynamic range have also been investigated [37].

The effect of input noise on a single–channel acoustooptic spectrum analyzer for a CW input signal is now analyzed. Next the analysis is extended to a multi–channel 2–D acoustooptic signal processor. The effect due to shot noise and detector noise is considered later.

9.1 Single–channel Bragg Cell Configuration

The output statistics for signal plus noise input on a single–channel acoustooptic spectrum analyzer using an integrating photodetector array have been derived [37–38]. Following a similar approach as given by Kelman et al[37] the effect of input Gaussian noise plus CW signal is analyzed in this section. The main difference from Kelman et al is that all the functions used in this analysis are two–dimensional in terms of the spatial coordinates (x,y) which represent the physical nature of an optical signal processor. In addition, the amplitude distribution in the Fourier plane is a single–sided Fourier transform of the input signal as given by Eq.(11), instead of a two–sided Fourier transform. There are also minor differences in the derived results which will be pointed out in the analysis.

The 2–D photodetector array is arranged in rows and columns and their numbers are designated by (i,j) respectively. The photodetector array is oriented with the row along the spatial frequency axis (x_1) and the column along the DOA axis (y_1). The spatial weighting function of each photodetector element is assumed to be identical and characterized by $H(x_1,y_1)$. The analysis is simplified by expressing the output from the 2–D photodetector array as a continuous distribution along the DOA axis. This is the same as assuming that the photodetector element row–to–row center spacing was infinitely small in

the y dimension and of rectangular spatial weighting. If the actual sampled spatial distribution from the 2–D photodetector array is needed, another integration along the DOA axis can be performed after.

For a single–channel acoustooptic spectrum analyzer, there is no useful information along the DOA axis and a linear photodetector array is used. In practice, the spreading of the signal distribution along the DOA axis is confined to the linear photodetector array by the use of a cylindrical lens. This is equivalent to performing an integration from minus infinity to plus infinity on the continuous output distribution of the 2–D photodetector array along the DOA axis. If a relative measurement is taken such as the signal–to–noise ratio, it can be carried out either on the continuous distribution or after performing the integration.

For an input acoustic CW signal of amplitude A and frequency f_s, the mean amplitude distribution in the column is computed by integrating the light intensity in both time and space. The light intensity is obtained by taking the square of the absolute value of the amplitude distribution given in Eq.(9). The mean output amplitude from photodetector column j is given by

$$\mu_{s,j}(y_1) = \int_{-\infty}^{\infty} H(x_1, y_1) \int_{t_o}^{t_o + T} \left| U_1[x_1 - (x_{1j} - x_{1s}), y_1, t] \right|^2 dt\, dx_1 \tag{68}$$

Let $G(x_1, y_1)$ be the magnitude squared of the Fourier transformed window function.

$$G(x_1, y_1) = \left| \iint_{-\infty}^{\infty} w(x_o, y_o) \exp[-j2\pi(\frac{1}{\lambda F} x_o + \frac{1}{\lambda F} y_o)] \, dx_o \, dy_o \right|^2 \tag{69}$$

and

$$\mathcal{H}(x_1, y_1) = \int_{-\infty}^{\infty} G(x_1 + x_1', y_1) \, H(x_1', y_1) \, dx_1' \tag{70}$$

be the correlation between the functions G and H. Following a similar analysis as given by Kelman et al, the mean output amplitude distribution of Eq.(68) can be shown to be

$$\mu_s(y_1) = (AK_3)^2/4 \; T \; \mathcal{H}(x_{1j} - x_{1s}, y_1) \tag{71}$$

where the spatial frequency point (x_1) are related to the input frequency by the use of Eq.(4) and Eq.(12) and thus x_{ij} and x_{is} correspond to frequencies

$$f_{s_j} = \frac{x_{1j}}{\lambda F} v_s \tag{72}$$

and

$$f_s = \frac{x_{1s}}{\lambda F} v_s \tag{73}$$

respectively , T is the integration period and

$$K_3 = K_B/(\lambda F) \tag{74}$$

There is one minor difference between the result given in Eq.(70) and that given by Kelman et al; $\mathcal{H}(x_1,y_1)$ is now defined as the correlation instead of convolution between the functions G and H. The end result is the same if the spatial weighting function of the photodetector element is symmetrical. However it is the view of the present author that correlation between the two functions is mathematically more correct.

The mean output noise power μ_η from photodetector column j is[37]

$$\mu_\eta(y_1) = \frac{\eta K_3^2}{2} T \int_{-\infty}^{\infty} G(x_1,y_1)\, dx_1 \int_{-\infty}^{\infty} H(x_1, y_1)\, dx_1 \tag{75}$$

The variance for noise only input for column j after the bias due to noise is subtracted is [37]

$$\sigma_\eta^2(y_1) = \left[\frac{\eta K_3^2}{2}\right]^2 T \int_{-\infty}^{\infty} \mathcal{H}^2(x_1,y_1)\, dx_1$$

$$= \left[\frac{\eta K_3^2}{2}\right]^2 T\, B_\eta\, \mathcal{H}^2(0,y_1) \tag{76}$$

where $B_\eta = \left[\int_{-\infty}^{\infty} \mathcal{H}^2(x_1,y_1)\, dx_1\right] / \mathcal{H}^2(0,y_1)$ (77)

is the noise equivalent bandwidth

For an input sinusoidal signal plus noise, if the integration period T is much larger than the acoustic transit time (τ) across the Bragg cell aperture D, then the variance at the output of column j is approximately given by [37]

$$\sigma^2_{s+\eta}(y_1) \approx \sigma^2_\eta(y_1)\left[1 + (AK_3)^2 \eta K_3^2 T\ \mathscr{H}^2(x_{1j} - x_{1s}, y_1)/[4\sigma^2_\eta(y_1)]\right] \tag{78}$$

Substituting $\sigma^2_\eta(y_1)$ from Eq (76) into the second term of Eq.(78)

$$\sigma^2_{s+\eta}(y_1) \approx \sigma^2_\eta(y_1)\left\{1 + (AK_3)^2 \eta K_3^2 T\ \mathscr{H}^2(x_{1j} - x_{1s}, y_1)/\left[4\left[\frac{\eta K_3^2}{2}\right]^2 TB_\eta \mathscr{H}^2(0,y_1)\right]\right\}$$

$$\approx \sigma^2_\eta(y_1)\left[1 + 2\,SNR_i\ \mathscr{H}^2(x_{1j} - x_{1s}, y_1)/\ \mathscr{H}^2(0,y_1)\right] \tag{79}$$

where

$$SNR_i = \left[(AK_3)^2/2\right] / \left[\eta K_3^2 B_\eta\right] = \left[A^2/2\right] / \left[\eta B_\eta\right] \tag{80}$$

is the input signal–to–noise ratio. The signal power is the total input signal power appearing in the Fourier plane and the noise is measured in the noise equivalent bandwidth B_η. There are two terms in Eq.(79) for the variance of the output. The first term is due to noise–noise mixing and the second term is due to signal mixing with noise. The second term has been expressed slightly different from Kelman et al [37]. It is now more general and takes into account that the signal can be located anywhere on the photodetector array. When the signal centroid is located off from the center of column j under consideration , a corresponding drop in the output signal–to–noise ratio will occur. Taking the ratio of the square of Eq.(71) to Eq.(76) , the output signal–to–noise ratio is

$$SNR_o = \mu^2_s(y_1)/\sigma^2_\eta(y_1)$$

$$= \left[[(AK_3)^2 T/4]^2\ \mathscr{H}^2(x_{1j} - x_{1s}, y_1)\right] / \left[[\eta K_3^2/2]^2 T\, B_\eta\ \mathscr{H}^2(0,y_1)\right]$$

$$= TB_\eta \left[SNR_i\ \mathscr{H}(x_{1j} - x_{1s}, y_1)/\mathscr{H}(0,y_1)\right]^2 \tag{81}$$

The output signal–to–noise ratio is directly proportional to the square of the effective input signal–to–noise ratio and the time–bandwidth product TB_η. The effective input signal–to–noise ratio is always less than or equal to the input signal–to–noise ratio given by Eq.(80) for a CW signal. An alternative definition of the output signal–to–noise ratio can be expressed as

$$\begin{aligned} SNR_o &= \mu^2_s(y_1)/\sigma^2_{s+\eta}(y_1) \\ &= \left[(AK_3)^2/4\ T\ \mathcal{H}(x_{1j}-x_{1s}, y_1)\right]^2 / \left[\sigma^2_\eta(y_1)[1 + 2\ SNR_i\, \mathcal{H}^2(x_{1j}-x_{1s}, y_1)/\ \mathcal{H}^2(0,y_1)]\right] \\ &= \frac{TB_\eta\ SNR_i^{\,2}\ \mathcal{H}^2(x_{1j}-x_{1s}, y_1)/\ \mathcal{H}^2(0,y_1)}{1 + 2\ SNR_i\, \mathcal{H}^2(x_{1j}-x_{1s}, y_1)/\ \mathcal{H}^2(0,y_1)} \end{aligned} \tag{82}$$

Again, there are two normalized terms appearing in the denominator of Eq.(80): the first one is due to noise–noise mixing and the second due to signal mixing with noise. The factor $\mathcal{H}^2(x_{1j}-x_{1s}, y_1)/\ \mathcal{H}^2(0,y_1)$ is always less or equal to unity for an input CW signal. As a result, the second term is dominant only for large input signal–to–noise ratios.

If $2\ SNR_i\, \mathcal{H}^2(x_{1j}-x_{1s}, y_1)/\ \mathcal{H}^2(0,y_1) \gg 1$, then

$$\mu^2_s(y_1)/\sigma^2_{s+\eta}(y_1) \approx TB_\eta\ SNR_i/2 \tag{83}$$

where it is noted that the signal–to–noise ratio is independent of the signal distribution and linearly proportional to the input signal–to–noise ratio. This is to be expected because now the noise is directly proportional to the signal due to the dominant product term of signal mixing with noise.

If $2\ SNR_i\, \mathcal{H}^2(x_{1j}-x_{1s}, y_1)/\ \mathcal{H}^2(0,y_1) \ll 1$, then

$$\mu^2_s(y_1)/\sigma^2_{s+\eta}(y_1) \approx TB_\eta \left[SNR_i\ \mathcal{H}(x_{1j}-x_{1s}, y_1)/\mathcal{H}(0,y_1)\right]^2 \tag{84}$$

As expected, the output signal–to–noise ratio is the same as for the case given by Eq.(81) because the noise contribution due to the presence of the signal is negligible. It is directly proportional to the product of the square of the effective input signal–to–noise ratio and TB_η.

When the noise–noise term is comparable with the term of signal mixing with noise, the output signal–to–noise ratio is given by Eq.(82). The output signal–to–noise ratio after being normalized by the time–bandwidth product is plotted in Fig.8 as a function of

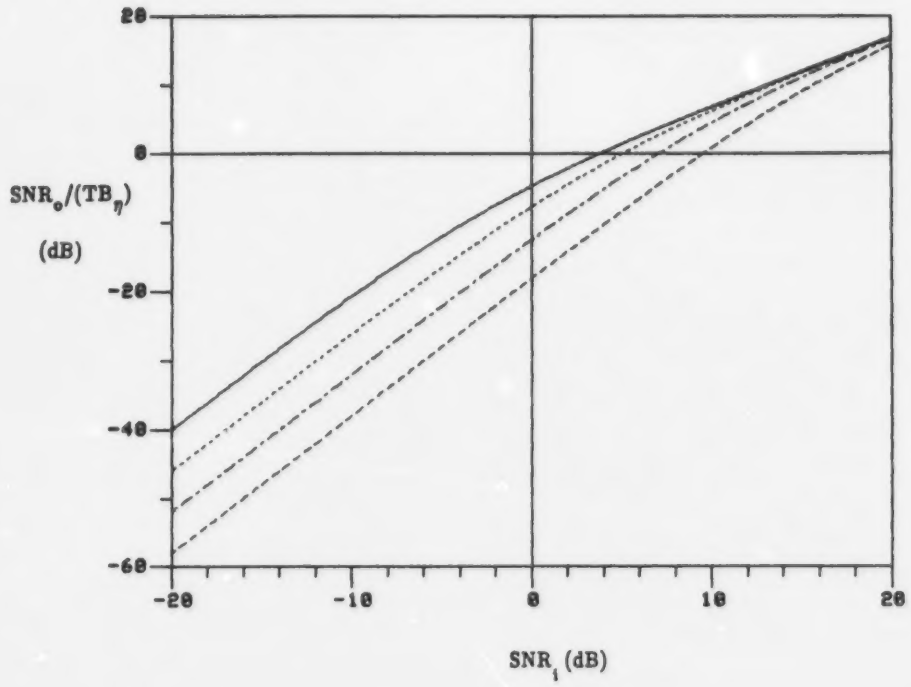

FIGURE 8: NORMALIZED OUTPUT SIGNAL–TO–NOISE RATIO VERSUS INPUT SIGNAL–TO–NOISE RATIO

(a) ———— $(x_{1j} - x_{1s}, y_1)/\ \mathscr{H}^2(0,y_1) = 1.0$

(b) ····· $(x_{1j} - x_{1s}, y_1)/\ \mathscr{H}^2(0,y_1) = 0.5$

(c) —·—·—·· $(x_{1j} - x_{1s}, y_1)/\ \mathscr{H}^2(0,y_1) = 0.25$

(d) -------- $(x_{1j} - x_{1s}, y_1)/\ \mathscr{H}^2(0,y_1) = 0.125$

the input signal–to–noise ratio and the ratio of $\mathscr{H}^2(x_{1j} - x_{1s}, y_1)/\ \mathscr{H}^2(0,y_1)$. Both the input and output signal–to–noise ratios are expressed in terms of their decibel equivalents. When the signal centroid is located at the center of the photodetector array column, the normalized output signal–to–noise ratio is – 4.77 dB for an input signal–to–noise ratio of 0 dB. For large input signal–to–noise ratios, it increases linearly with the input signal–to–noise ratio as given by Eq.(83) and independent of the ratio of $\mathscr{H}^2(x_{1j} - x_{1s}, y_1)/\ \mathscr{H}^2(0,y_1)$. For low input signal–to–noise ratio, it is directly proportional to the square of the effective input signal–to–noise ratio.

The processing gain may be defined as the ratio of the input signal–to–noise ratio without integration to the input signal–to–noise ratio with integration in order to achieve the same detection probability. From Eq.(81) and Eq.(82) for low input signal–to–noise ratio, the peak processing gain is found to be proportional to $\sqrt{TB_\eta}$.

9.2 Multi–channel Bragg Cell Configuration

The effect of input Gaussian noise has been analyzed for a sinusoidal input signal on a single channel acoustooptic spectrum analyzer. This analysis is now extended to a multi–channel configuration. The noise statistics in each channel are assumed to be the same but uncorrelated from channel to channel, and the window weighting function is assumed to be the same for each channel.

The mean amplitude distribution in column j for an input sinusoidal signal alone is given by Eq.(71) for a single–channel configuration. For a N–channel configuration, it is modified by the array factor as

$$\mu_{s,N}(y_1) = \left| N\, f(y_1) \right|^2 (AK_3)^2/4\ T\ \mathscr{H}(x_{1j} - x_{1s}, y_1), \tag{85}$$

where $f(y_1)$ is the normalized array factor given by Eq.(21). The maximum amplitude is N^2 times that of a single–channel one and the distribution along the column is now a function of the array factor. The mean output noise power μ_η is

$$\mu_{\eta,N}(y_1) = \sum_{n=1}^{N} \eta_n\, K_3{}^2/2\ T \int_{-\infty}^{\infty} G(x_1,y_1)\, dx_1 \int_{-\infty}^{\infty} H(x_1, y_1)\, dx_1 \tag{86}$$

where the above equation shows that the output mean for the N–channel configuration for noise input alone is the sum of the individual mean values. This is due to the fact that the noise in each channel is uncorrelated.

For noise only input, the variance after the bias due to noise is subtracted can be shown to be

$$\sigma^2_{\eta,N}(y_1) = \left[\sum_{n=1}^{N} \eta_n \frac{K_3^2}{2} \right]^2 T B_\eta \mathscr{H}^2(0,y_1) \tag{87}$$

For an input sinusoidal signal plus noise, the analysis as given by Kelman et al[37] for a single–channel configuration can be extended to a N–channel one. The variance at the output of column j is obtained as

$$\sigma^2_{s+\eta,N}(y_1) \approx \sigma^2_{\eta,N}(y_1) \left[1 + \left| N f(y_1) \right|^2 (AK_3)^2 \sum_{n=1}^{N} \eta_n K_3^2 T \mathscr{H}^2(x_{1j} - x_{1s}, y_1) \right.$$

$$\left. /[4\sigma^2_{\eta,N}(y_1)] \right] \tag{88}$$

If the signal and noise amplitudes are identical from channel to channel , then

$$\sigma^2_{s+\eta,N}(y_1) \approx N^2 \sigma^2_{\eta}(y_1) \left[1 + 2\, SNR_{i,N} \mathscr{H}^2(x_{1j} - x_{1s}, y_1) / \mathscr{H}^2(0,y_1) \right] \tag{89}$$

where

$$SNR_{i,N} = \left[[N \left| f(y_1) \right| A]^2/2 \right] / \left[N\eta B_\eta \right] = N \left| f(y_1) \right|^2 SNR_i \tag{90}$$

is the effective input signal–to–noise ratio appearing in the Fourier plane of a N–channel configuration and SNR_i is the input signal–to–noise ratio for a single–channel configuration given by Eq.(80). The peak input signal–to–noise ratio is N times that of the single–channel configuration. The output signal–to–noise ratio is

$$SNR_o = \mu^2_{s,N}(y_1)/\sigma^2_{\eta,N}(y_1)$$

$$= \left[\{ [\left| N f(y_1) \right|^2 AK_3]^2 T/4 \}^2 \mathscr{H}^2 (x_{1j} - x_{1s}, y_1) \right] / \left[[N\eta K_3^2/2]^2 T B_\eta \mathscr{H}^2(0,y_1) \right]$$

$$= TB_\eta \left[SNR_{i,N} \mathscr{H}(x_{1j} - x_{1s}, y_1) / \mathscr{H}(0,y_1) \right]^2 \tag{91}$$

An alternative definition for the output signal–to–noise ratio is

$$SNR_o = \mu^2_{s,N}(y_1)/\sigma^2_{s+\eta,N}(y_1)$$

$$= \left[\left[\left| N f(y_1) \right|^2 A K_3 \right]^2 / 4 T \mathcal{H}(x_{ij} - x_{1s}, y_1) \right]^2 / \left[N^2 \sigma_\eta^2(y_1) \cdot \left[1 + 2 SNR_{i,N} \mathcal{H}^2(x_{ij} - x_{1s}, y_1) / \mathcal{H}^2(0, y_1) \right] \right]$$

$$= \frac{TB_\eta SNR_{i,N}^2 \mathcal{H}^2(x_{ij} - x_{1s}, y_1) / \mathcal{H}^2(0, y_1)}{1 + 2 SNR_{i,N} \mathcal{H}^2(x_{ij} - x_{1s}, y_1) / \mathcal{H}^2(0, y_1)} \tag{92}$$

If $2 SNR_{i,N} \mathcal{H}^2(x_{ij} - x_{1s}, y_1) / \mathcal{H}^2(0, y_1) << 1$, then

$$\mu_s^2(y_1) / \sigma_{s+\eta}^2(y_1) \approx TB_\eta \left[SNR_{i,N} \mathcal{H}(x_{ij} - x_{1s}, y_1) / \mathcal{H}(0, y_1) \right]^2 \tag{93}$$

If $2 SNR_{i,N} \mathcal{H}^2(x_{ij} - x_{1s}, y_1) / \mathcal{H}^2(0, y_1) >> 1$, then

$$\mu_s^2(y_1) / \sigma_{s+\eta}^2(y_1) \approx TB_\eta SNR_{i,N} / 2 \tag{94}$$

By comparing the output signal–to–noise ratios given by Eqs.(91 to 94) for a N–channel configuration to those given by Eqs.(81 to 84) for a single–channel configuration, the only difference is the effective input signal–to–noise ratio. For the N–channel configuration it is modified by N times the square of the normalized array factor. As a result for low effective input signal–to–noise ratios, the maximum output signal–to–noise ratio is improved by a factor of N^2. For comparison, we define another processing gain as the ratio of the input signal–to–noise ratio for a single–channel Bragg cell configuration to the input signal–to–noise ratio for a N–channel one in order to achieve the same detection probability. From Eq.(81) and Eq.(91) for low input signal–to–noise ratios, the peak processing gain is found to be proportional to N.

The analysis has been carried out for the case where the input noise is dominated by the receiver noise with an input CW signal. However the output sampled data value also includes an additive detection noise contribution [37]. Detection noise has both thermal and shot components. Shot noise depends on the average optical power and is therefore signal dependent. Thermal noise, due to random agitation of electrons and reset charge uncertainty, is independent of the optical signal. The relative importance of thermal versus shot noise depends on the number of photo electrons. It has been shown that shot noise effects are negligible for devices with more than several hundred rms thermal noise electrons. As shown by Kelman et al[37], if the receiver noise is set to about the same level as the thermal noise, and for time–bandwidth products not extremely large, the effect of shot noise can be neglected. At low input signal levels, the shot noise generated is negligible in comparison with both the thermal and receiver noise. At high input signal level, the shot noise increases linearly with the input signal level, however the noise generated by the signal and input noise as given by Eq.(88) will dominate. As a result, shot noise effect can be neglected.

The distribution of the combined noise is approximately Gaussian for large time–bandwidth product with large output signal amplitude [37–38]. In addition the output DOA pattern is usually digitized for further analysis and processing and thus quantization error will also be introduced. The different sources of error can be added on the basis of their RMS values. To perform the most accurate estimate of peak location, it is best to maximize the signal energy collected and at the same time minimize the noise[39]. For the 2–D acoustooptic signal processor, the sampled DOA pattern can be further processed to obtain sub–pixel resolution through digital interpolation[40]. The ultimate optimum peak locator or estimator[39,41] to be used will be in general a function of the input signal, the interpolation technique used and the pixel size.

10.0 COMPARISON BETWEEN MICROWAVE AND OPTICAL ARRAY PATTERNS

The DOA pattern of the optical configuration can also be split into a product of two functions: the element pattern and the array pattern.

The element pattern is determined by the interacting profile of the acoustic column and the laser beam. The effect of the element pattern on the DOA pattern has been presented in Section 6.0. The DOA pattern distribution of the optical array factor is a continuous function of the spatial coordinate with no bounds on the range of y_1. In other words, there are no "invisible" regions as in the case of a microwave antenna array pattern. For the linear antenna array configuration, the microwave antenna array factor pattern is a function of $\sin(\theta)$ which is periodic and within the range of ± 1. For the circular antenna array configuration, it is periodic and within the range of $\theta = \pm 180$ degrees.

The shape of the optical array DOA pattern is unchanged by the phase tilt introduced when the signal arrives off boresight. Only the center or beam axis is altered. However, for the linear antenna array configuration, the radiation pattern of the microwave antenna array is distorted due to the trigonometric transformation relating the variables y_1 and θ.

11.0 DESIGN CRITERIA USING A LINEAR ANTENNA ARRAY

11.1 Linear Periodic Array Versus Aperiodic Array

The condition to avoid grating lobes under all conditions of beam–steering for a linear periodic array is [30]

$$d \leq \lambda_R/2 \tag{95}$$

where d is the element spacing and λ_R is the wavelength of the received signal.

Two important implications follow, the first pertaining to cost and the second to mutual coupling. The cost of a linear array with its separate RF channels is approximately proportional to the length $2\ell_N$. The resolving power of the array or its beamwidth is always proportional to the length $2\ell_N$. The angular resolution is just a function of the

length of the array and not the number or distribution of elements. The effect of mutual coupling on closely spaced elements is another factor. The effect of mutual coupling among antenna elements can be reduced by overspacing the elements in the array, a process known as thinning. This process will introduce grating lobes unless the array is made nonperiodic. The problem of a thin array is the reduction of the designer's control of the radiation pattern in the sidelobe region. This arises because of its reduced number of elements, which offers the designer fewer degrees of design freedom than a filled array. There exists no single theory which governs the design of an aperiodic array [30]. With the exception of a random array, aperiodic arrays are designed ad hoc. Various design techniques for the aperiodic arrays have appeared in the literature to reduce the large sidelobes [42],[43], but the success has been quite limited.

Equal gain channels are highly practical in terms of design, manufacture and optimum use of components. For broadband receiver designs, the physical size of the antenna may be a constraint in which the antenna diameter may not satisfy the requirement given by Eq. (95). In order to keep the number of channels to a reasonable number while still having some control over the main lobe width and sidelobe levels, four to five antenna elements with unequal spacings seem to be the optimum number.

11.2 Design Example

An example is given on the synthesis of an array using four nonuniformly spaced elements of equal weighting.

Consider a design where it is desirable to cover the frequency range of 6.0 to 12.5 GHz. The bearing accuracy is to be in the order of 1 degree for the worst case of 30 degrees RMS phase and 3 dB power imbalances. The total instantaneous angular field–of–view is chosen as ± 45 degrees in order to provide a system to cover one quadrant in azimuth.

The main design criteria used are:

(i) To minimize the main lobe width while the peak sidelobe–to––main–lobe ratio is kept to a reasonable minimum.

(ii) To optimize the channel spacings so that the ratio of the peak sidelobe–to–main–lobe level is least sensitive to perturbations of channel locations.

The beam pointing error is inversely proportional to the length of the baseline as given by Eq. (59) while the angular resolution is directly proportional to it. It is also well known that the peak sidelobe–to–main–lobe ratio is less susceptible to channel spacing variations for a longer baseline. On the other hand, the difficulty in controlling the peak sidelobe–to–main–lobe ratio for a given number of channels is directly proportional to the length of the baseline. As a result, a compromise has to be made.

In order to realize the array, antenna elements and acoustic columns are chosen to be separated as far apart from each other as possible for ease of fabrication and reduction of mutual coupling effects.

Giving the specified system phase and amplitude errors and the required pointing error, the total baseline length can be determined from Eqs.(57) and (66). Let's consider a baseline length of about 10.5 wavelengths at 12.5 GHz, there are up to 15 sidelobes on

either side of the main lobe within the scanning angular range of ±45 degrees. Since there are only two degrees of freedom corresponding to the inner two element locations, at least two sidelobes out of the possible 15 can be optimized. However, no matter which algorithmic design is used, it is going to have little control of the radiation pattern in this case.

On the other hand, since there are only four channels, the optimum locations of the inner two channels can be determined by using a computer. This is done by moving the two inner channels, one at a time, in discrete steps within the baseline and recording the main–lobe–to–peak sidelobe ratio within the scanning angular range of ± 45 degrees. A two–dimensional grid table, showing the peak sidelobe–to–main–lobe ratio as a function of the two inner channel spacings, is used to determine the optimum channel spacings. By the conservation of radiation energy, keeping the peak sidelobes to a minimum value has more or less the same effect of trying to equalize the sidelobe levels. It is found that there are various regions of minima of different sizes. The purpose is to identify some of the largest regions of about the same length and width so that the two–dimensional table can be reduced to a number of smaller and more manageable elements. Once an optimum 2–D table is identified, the locations of the two end elements can then be perturbed to form another 2–D table. It is to be noted that the resultant DOA pattern is a vector sum of the four vectors rotating at different rates as the scanning angle is varied. For small perturbations, that is for small grid size steps, the peak sidelobe–to–main–lobe level is expected to vary smoothly from grid point to grid point even though the location where the peak sidelobe occurs may be changed. As a result, once an optimum region is identified and with slight perturbations, the optimum region should only be slightly perturbed as well. This characteristic will be illustrated in this design example.

An optimum 2–D table is shown in Table I for this specific example of a 10.5 wavelength baseline at 12.5 GHz. The initial optimum element spacings are found to be at 0.0 3.7 6.25 and 10.5 wavelengths. Next the two inner element locations are fixed with the outer two elements perturbed and the resultant 2–D grid table is shown in Table II. As expected, the minimum peak sidelobe–to–main–lobe level is already at around its minimum for small perturbations around the optimum element locations. In order to get an idea on what will happen to the original peak sidelobe–to–main–lobe distribution as the two end locations are changed, two other grid points around the optimum will be chosen. In addition, we want to emphasize that only the outer two element positions are perturbed, and as a result, the coordinates for the inner element locations will be kept unchanged. As the outer two element locations are changed, so will the total baseline length. From Table II, another grid point at $d_1 = -0.0625$ and $d_4 = 10.5625$ wavelengths is selected. This corresponds to a longer baseline length of 10.625 wavelengths and another grid table is shown in Table III by perturbing element locations d_2 and d_3. By comparing Table III to Table I, a similar optimum region is obtained. It has confirmed the notion that for small perturbations around the optimum locations, the optimum region should only be slightly perturbed. Another grid point at $d_1 = 0.0625$ and $d_4 = 10.375$ with a total baseline length of 10.3125 wavelengths is chosen and another grid table is shown in Table IV. As expected, a similar optimum table is obtained. The above two cases have confirmed that the optimum element locations as calculated in Table I are still the optimum locations. By using finer grid sizes to locate the centroid of the minimum region and rounding the element locations to two decimal points, the optimum element locations are found to be at –5.25 –1.54, 0.98 and 5.25 and the peak sidelobe–to–main–lobe ratio is 0.69. An optimum region has been found where the peak sidelobe to main lobe ratio is least sensitive to element location perturbations and thus to phase errors as well.

TABLE I

OPTIMUM TABLE SHOWING THE PEAK SIDELOBE–TO–MAIN–LOBE VALUES FOR AN ARRAY OF 10.5 WAVELENGTHS LONG

($d_1 = 0\ \lambda_R$ and $d_4 = 10.5\ \lambda_R$)

	d_2 (λ_R)						
d_3 (λ_R)	3.8875	3.8250	3.7625	3.7000	3.6375	3.5750	3.5125
6.4375	.94	.92	.87	.80	.80	.82	.83
6.3750	.87	.86	.82	.76	.76	.89	.93
6.3125	.85	.79	.75	.70	.77	.93	1.00
6.2500	.86	.81	.74	.68	.79	.86	.96
6.1875	.86	.81	.75	.71	.85	.94	.97
6.1250	.86	.82	.82	.75	.84	.95	1.00
6.0625	.84	.92	.95	.90	.76	.89	.96

TABLE II

OPTIMUM TABLE SHOWING THE PEAK SIDELOBE–TO–MAIN–LOBE VALUES FOR AN ARRAY OF 10.5 WAVELENGTHS LONG

($d_2 = 3.7\ \lambda_R$ and $d_3 = 6.25\ \lambda_R$)

	d_1 (λ_R)						
d_4 (λ_R)	0.1875	0.1250	0.0625	0.0000	–0.0625	–0.1250	–0.1875
10.6875	.96	.95	.91	.85	.77	.70	.74
10.6250	.98	.95	.89	.81	.71	.72	.76
10.5625	.97	.92	.85	.75	.70	.74	.77
10.5000	.95	.88	.78	.68	.71	.75	.80
10.4375	.89	.81	.70	.69	.75	.81	.85
10.3750	.82	.72	.69	.75	.81	.86	.90
10.3125	.73	.70	.75	.81	.87	.91	.94

TABLE III

OPTIMUM TABLE SHOWING THE PEAK SIDELOBE–TO–MAIN–LOBE VALUES FOR AN ARRAY OF 10.625 WAVELENGTHS LONG

($d_1 = -0.0625\ \lambda_R$ and $d_4 = 10.5625\ \lambda_R$)

	d_2 (λ_R)						
d_3 (λ_R)	3.8875	3.8250	3.7625	3.7000	3.6375	3.5750	3.5125
6.4375	.93	.92	.88	.81	.78	.80	.82
6.3750	.85	.85	.82	.77	.74	.87	.95
6.3125	.87	.81	.75	.70	.70	.88	.98
6.2500	.88	.82	.76	.70	.77	.86	.91
6.1875	.88	.83	.77	.71	.81	.92	.97
6.1250	.86	.82	.86	.81	.79	.91	.99
6.0625	.84	.90	.97	.94	.83	.84	.93

TABLE IV

OPTIMUM TABLE SHOWING THE PEAK SIDELOBE–TO–MAIN–LOBE VALUES FOR AN ARRAY OF 10.3125 WAVELENGTHS LONG

($d_1 = 0.0625\ \lambda_R$ and $d_4 = 10.3750\ \lambda_R$)

	d_2 (λ_R)						
d_3 (λ_R)	3.8875	3.8250	3.7625	3.7000	3.6375	3.5750	3.5125
6.4375	.98	.95	.89	.81	.83	.84	.86
6.3750	.93	.91	.87	.80	.79	.81	.82
6.3125	.86	.85	.81	.75	.75	.77	.80
6.2500	.86	.80	.74	.69	.71	.76	.81
6.1875	.87	.81	.75	.69	.81	.88	.89
6.1250	.87	.82	.76	.70	.85	.95	.98
6.0625	.86	.84	.87	.80	.82	.94	.99

The normalized optical intensity patterns of the array are plotted in Fig.9 for both a signal arriving on boresight with no errors and for one with 30 degrees RMS phase error and 3 dB power error. Since the patterns are symmetrical, only one side is shown. It is to be noted that there is a distinction between the antenna radiation pattern and the DOA pattern as described in Section 10 and care should be taken in the design of the optimum array. If a photodetector array is used to spatially sample the DOA pattern for the angular field–of–view of ±45 degrees, it must have a minimum length of equivalent to 2 times $\sin(45^\circ) = 1.4142$ in the y_2 coordinate. If a signal is received at 45 degrees off boresight, the DOA pattern will be shifted by 0.7071 units in terms of y_2. Now the sidelobes located within $y_2 = 1.4142$ will be shifted to the visible region and detected by the photodetector array as shown in Fig.9. This is different from the radiation pattern of the corresponding antenna array where for the same field–of–view of ±45 degrees, only the pattern extending from ± 90 degrees are of interest or when expressed in terms of $\sin(\theta)$, which is within the range of ±1. In other words, in the design of an array which can span the ±45 degrees field–of–view, the sidelobes located beyond the ± 1 and out to ± 1.4142 have to be considered when determining the potential peak side–lobe–to–main–lobe ratio for the scanning angular range of ± 45 degrees.

The interaction profile between the acoustic column and laser is assumed to be of uniform width ($\ell_N/30$). From Eqs.(57) and (66), the RMS pointing errors for a 30 degrees RMS phase error are 1.30 degrees and 0.63 degrees at 6.0 and 12.5 GHz respectively. The worst case peak sidelobe–to–main–lobe ratio is 0.69. The 3 dB beamwidths of the array factor are 8.0 degrees and 3.8 degrees at 6 and 12.5 GHz respectively. The ratio of the total 3–dB beamwidth power to total power is 0.056. A photodetector array is usually used for detection and interpolation is employed to obtain about 1 degree angular resolution.

An experimental 2–D acoustooptic receiver based on the above design concept has been completed. This experimental receiver has been evaluated extensively using simulated and radiated signals[44]. Some experimental measurements on the amplitude and phase tracking characteristics of a multi–channel an isotropic Bragg cell on lithium niobate has also been reported [45].

Now the effect of the input Gaussian illumination profile parameter Ty on the DOA pattern is analyzed. As mentioned in Section 7.1, that a maximum in the total optical power interacting with the acoustic beams usually may not result in a maximum main lobe intensity on the DOA pattern. This effect is illustrated in this section by using the optimum designed 4–channel spacings. In this case, the optimum relative acoustic array spacings are as follows:

$$\begin{aligned} \ell_1 &= -\ell_4 \\ \ell_2 &= -0.2933\ \ell_4 \\ \ell_3 &= 0.1867\ \ell_4 \end{aligned} \tag{96}$$

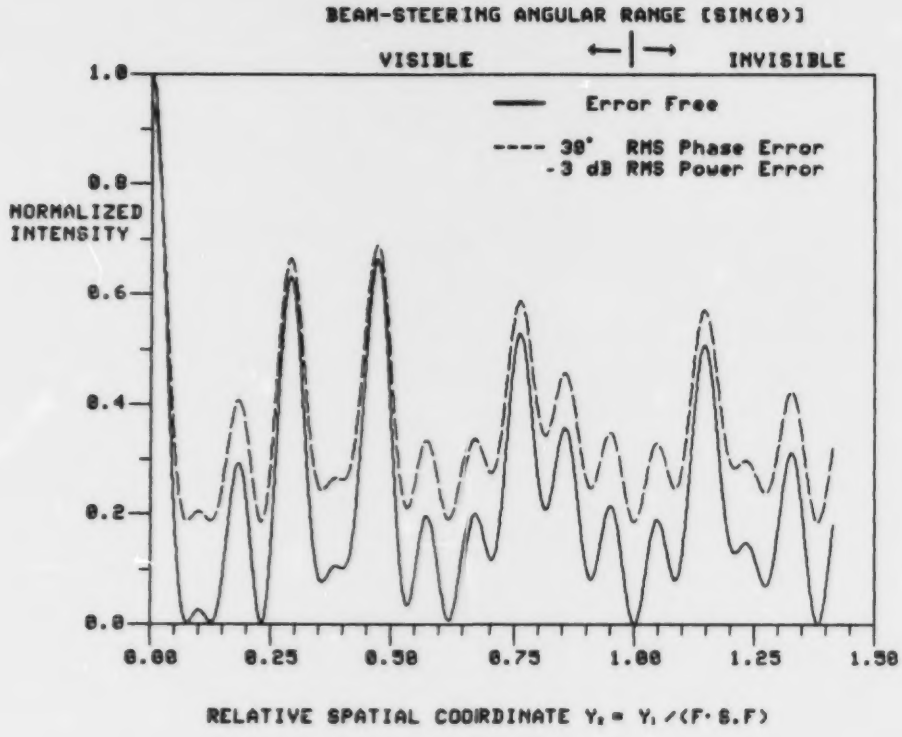

FIGURE 9: NORMALIZED INTENSITY PATTERN OF AN OPTIMUM APERIODIC ARRAY [Base line = 10.5 λ_R at 12.5 GHz; Element locations(λ_R): −5.25, −1.54, 0.98, and 5.25, $\bar{H} = \ell_N/30$]

In this case, a laser with a total power of unity is used to illuminate the 4–channel Bragg cell fully. The illumination profile is of Gaussian distribution characterized by the parameter Ty. Using Eq.(47), the normalized total power interacting with the four acoustic beams is plotted in Fig. 10, curve (a), as a function of the Gaussian profile Ty. For Ty close to zero, the Gaussian beam is very large in comparison with the acoustic array and thus a very small portion of the input laser power is utilized in the interaction. As the Gaussian beamwidth is decreased, more and more of the input laser power is utilized, and depending on the acoustic channel locations, a number of maxima may occur. For this specific 4–element array, the first maximum occurs at around Ty = 2.14. The resultant relative maximum intensity of the main lobe level of the DOA pattern is also plotted in Fig. 10, curve b, as a function of Ty. However, by comparing the two plots, the maximum main lobe intensity occurs at Ty = 0.8, and the two curves are different in shape. We are only interested in small Ty because the main lobe width of the DOA pattern increases with Ty and thus will result in a reduction of the angular resolution of the processor. At Ty = 0.8, where the maximum main lobe intensity occurs, we have the following relative amplitude distribution in the four acoustic channels,

$$\begin{aligned} a_1 = a_4 &= 0.092 \\ a_2 &= 0.165 \\ a_3 &= 0.170 \end{aligned} \tag{97}$$

The relative maximum intensity of the main lobe is

$$(a_1 + a_2 + a_3 + a_4)^2 = 0.27 \tag{98}$$

while the maximum total laser power interacting with the four acoustic beams is

$$a_1^2 + a_2^2 + a_3^2 + a_4^2 = 0.073 \tag{99}$$

out of a total maximum of unity.

For comparison, a rectangular laser profile with a width of $(2\,\ell_4 + H)$ in the y dimension, and having the same total power is used. The transformation of the Gaussian beam into a rectangular beam could be performed using a holographic filter [46]. If we assume that the transformation were 100% efficient, and the acoustic beams were self–collimating, the maximum total laser power interacting with the acoustic beams would have a value of $0.0232 \times 4 = 0.093$. The relative maximum intensity of the main lobe would have a value of 0.37 which is 1.38 times that of the case where the optimum Gaussian illumination of Ty = 0.8 is used.

The DOA patterns for the two cases, rectangular weighting and optimum Gaussian weighting, are plotted in Fig. 11 for a signal arriving on boresight. The maximum values of the two cases have been normalized to a value of unity. As expected, the Gaussian weighting has the effect of broadening the main lobe and suppressing the sidelobe levels.

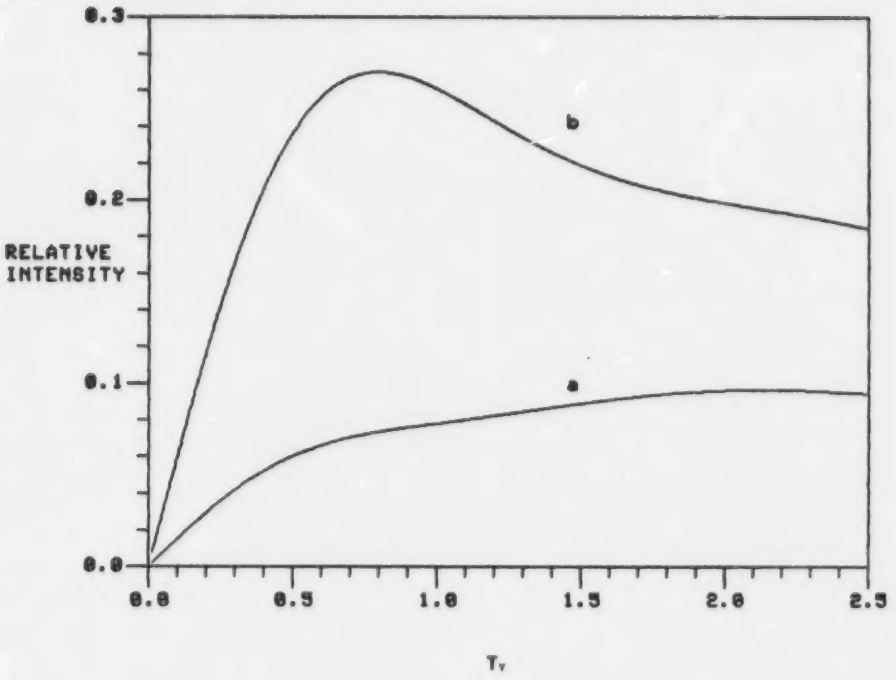

FIGURE 10: TOTAL INTERACTING OPTICAL INTENSITY AND ITS PEAK DOA INTENSITY VERSUS Ty FOR AN OPTIMUM APERIODIC ARRAY

(a) Total Optical Intensity Utilized in the Interaction with Acoustic Beams

(b) Relative Peak Intensity of DOA Pattern

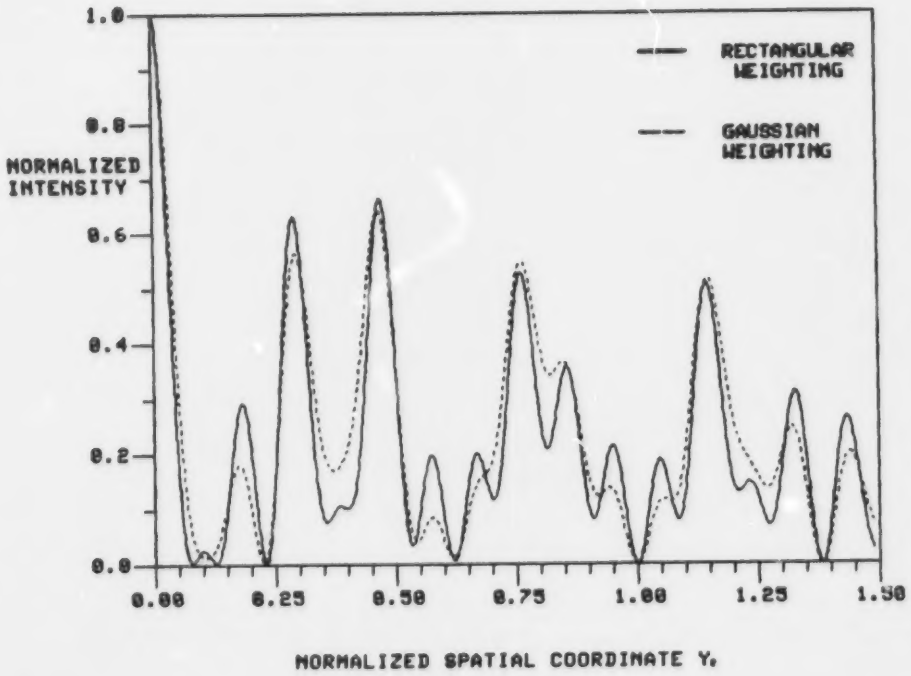

FIGURE 11: NORMALIZED DOA PATTERN OF AN OPTIMUM 4–CHANNEL APERIODIC ARRAY ILLUMINATED WITH

(a) ———— Rectangular Weighting

(b) ..... Optimum Gaussian Weighting (Ty = 0.8)

12.0 DESIGN CRITERIA USING A CIRCULAR ANTENNA ARRAY WITH A BUTLER MATRIX

A feasible architecture, using a 32–element circular antenna array and a Butler matrix with 9 output ports of n = 0 , ±1 ,± 2, ± 3, ± 4, is shown in Fig. 7. The ideal DOA patterns for both a rectangular and Gaussian illumination weightings are shown in Fig.12. As can be seen from the plot, Gaussian amplitude weighting has a strong effect in suppressing the sidelobe level for a periodic array configuration. It is to be noted that the shape of the ideal DOA pattern is independent of signal frequency . If the incoming signal is received off boresight, the DOA pattern will be shifted in position and the location of the peak pattern will give a direct measure of bearing, independent of frequency. In addition, the bearing accuracy is shown to be relatively insensitive to small elevation angle variations [47]. The 32–element array with a Butler matrix has been employed by Anaren Inc. in their Radar ESM systems for years [47]. However, the phase offset relationship as given by Eq.(24) is not yet fully satisfied and the output ports of n = ± 3 are not available.

There are a number of advantages of using a filled acoustic array of periodic arrangement in this configuration. As shown in Fig 12, Gaussian amplitude weighting profile from a laser can be effectively utilized for the reduction of sidelobe levels on the DOA pattern. Moreover, the multi–channel Bragg cell can be illuminated efficiently without the use of beam–splitting optics such as holographic lens elements which may introduce additional distortion and loss [48]. As a result, the filled array configuration is investigated in detail.

The effect of Gaussian illumination profile on maximizing the output peak DOA pattern is investigated first. The Gaussian profile along the DOA axis is completely characterized in Eq.(46) by the parameter Ty. To maximize the sidelobe suppression effect, the laser profile is chosen to be centrally located with respect to the array center. The total effective interacting laser power is that portion of the input laser power which is utilized in the interaction with the acoustic beams. It is plotted in Fig.13 as a function of Ty for a N–channel configuration with H/ℓ equals 0.2. H/ℓ is the ratio of the transducer height to the transducer center–to–center separation. The smallest array is the 2–element array with one channel fed by mode 0 and the other by either mode = 1 or –1. As the number of channel is increased, more and more channels are added to either side of the array. The Gaussian illumination profile is expanded to accommodate this increase in the baseline length. For N even, a maximum is reached at some finite value of Ty. As can be seen from the plot, for N = 2, a maximum is obtained at Ty = 0.5. For N odd, a maximum is reached at Ty approaching infinity. The resultant relative peak main lobe intensity of the output DOA pattern can be computed by using Eq.(47) and plotted in Fig.14. The optimum Ty which produces a maximum output peak intensity is marked by a circle in Fig.14. Since both H and ℓ are the same for each configuration, the resultant peak intensity increases with the square of (N–1) for the increase in the number of channels, while the input illumination intensity is inversely proportional to (N–1). As a result, the net increase in the relative peak intensity is approximately proportional to (N–1). By comparing Fig. 13 to Fig. 14, it is noted that a maximum in the total interacting power, with the exception of N = 2, does not correspond to a maximum output peak intensity on the DOA pattern. Near the optimum Ty region, the output intensity is shown to be relatively insensitive to variations in Ty. Similar plots have also been obtained for different H/ℓ ratios and the shape is about the same while the relative magnitude increases directly proportional to H/ℓ .

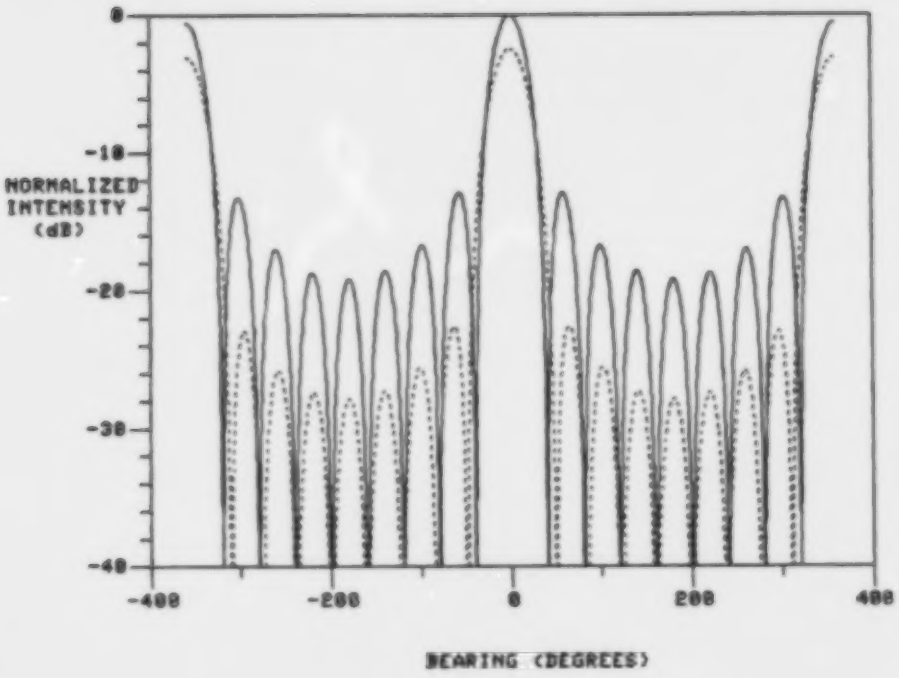

FIGURE 12: NORMALIZED DOA PATTERN OF A 9–CHANNEL RECEIVER USING A CIRCULAR ANTENNA ARRAY

(a) ———— Ty = 0, $H/\ell = 0.2$

(b) ..... Ty = 0.88, $H/\ell = 0.2$

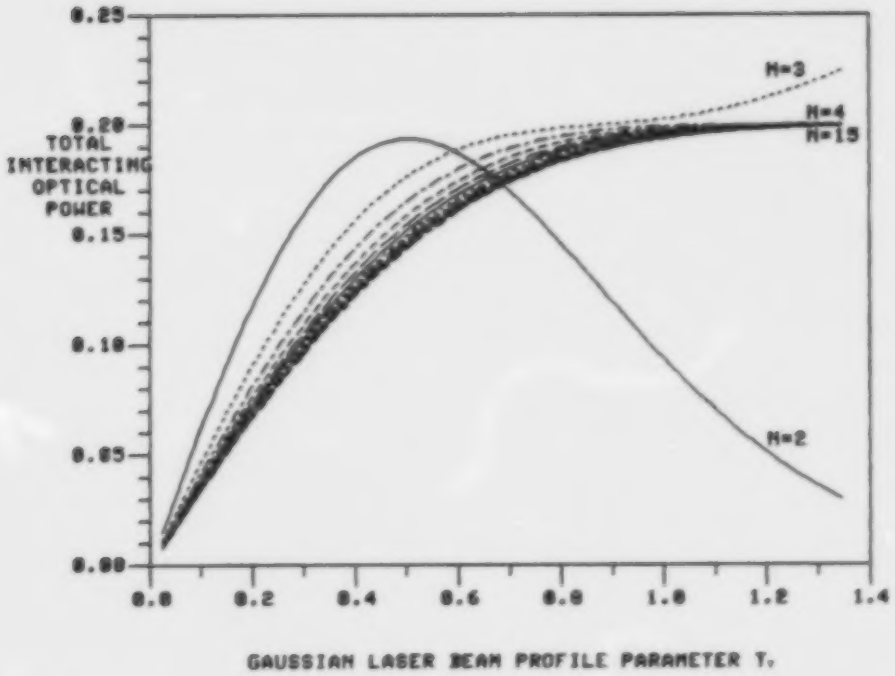

FIGURE 13: TOTAL INTERACTING OPTICAL POWER VERSUS Ty FOR A N–CHANNEL RECEIVER USING A CIRCULAR ANTENNA ARRAY ($H/\ell = 0.2$)

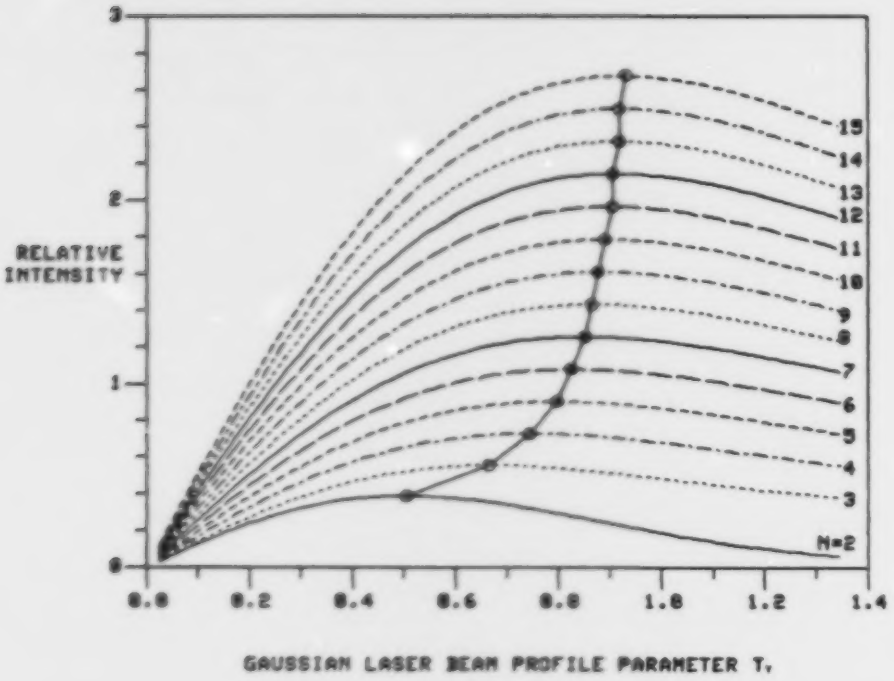

FIGURE 14: RELATIVE PEAK INTENSITY OF DOA PATTERN VERSUS Ty FOR A N–CHANNEL RECEIVER USING A CIRCULAR ANTENNA ARRAY ($H/\ell = 0.2$)

In addition to the maximum output peak value of the DOA pattern, other parameters such as the main beamwidth and sidelobe levels are also of importance. The 3–dB beamwidth as a function of Ty is plotted in Fig.15, for $H/\ell = 0.2$. As can be seen in the graph, the beamwidth is inversely proportional to the baseline length or to (N–1), where N is the number of channels. The Gaussian profile is shown to have the effect of broadening the beamwidth. It is also found that the 3–dB beamwidth is insensitive to the ratio H/ℓ, as long as $(N-1)\ell >> H$. The peak sidelobe level within the range of ± 360 degrees, which includes all the possible patterns when the signal is received over the 360–degree field–of–view, is plotted in Fig.16. The secondary peaks located at 360 degrees on either side of main lobe have been discarded and thus are not counted as sidelobes in the plot. In some cases, there are no sidelobes produced on the DOA pattern and the null is taken to be the peak sidelobe level. As can be seen from the graph, the Gaussian weighting has the effect of suppressing the sidelobe levels and this suppression effect increases with Ty. It is also found to be insensitive to H/ℓ , for $(N-1)\ell >> H$.

Another parameter on the ratio of the total power contained in the 3–dB beamwidth to the total power in the DOA pattern as a function of Ty, is also of interest. This parameter gives an indication of how much of the useful diffraction power is contained in the main lobe of the DOA pattern. This ratio is plotted in Fig.17 for $H/\ell = 0.2$.

Making use of Eqs.(60) and (62) , the RMS pointing error of the received signal is approximately given by

$$\sigma_{(\theta-\theta_o)} = \frac{\sigma_\phi \ell \left[\sum_{n=1}^{N} a_n^2 \ell_n^2 \right]^{1/2}}{2\pi \sum_{n=1}^{N} a_n \ell_n^2} \tag{100}$$

For a filled array of N elements, the total acoustic array length is $(N-1)\ell$. Normalizing the element location by the total acoustic array length in the above equation, we have

$$\sigma_{(\theta-\theta_o)} = \frac{\sigma_\phi \left[\sum_{n=1}^{N} a_n^2 \ell'^2_n \right]^{1/2}}{2\pi (N-1) \sum_{n=1}^{N} a_n \ell'^2_n} \tag{101}$$

$$\text{or} \qquad = P.F\ \sigma_\phi / [2\pi (N-1)] \tag{102}$$

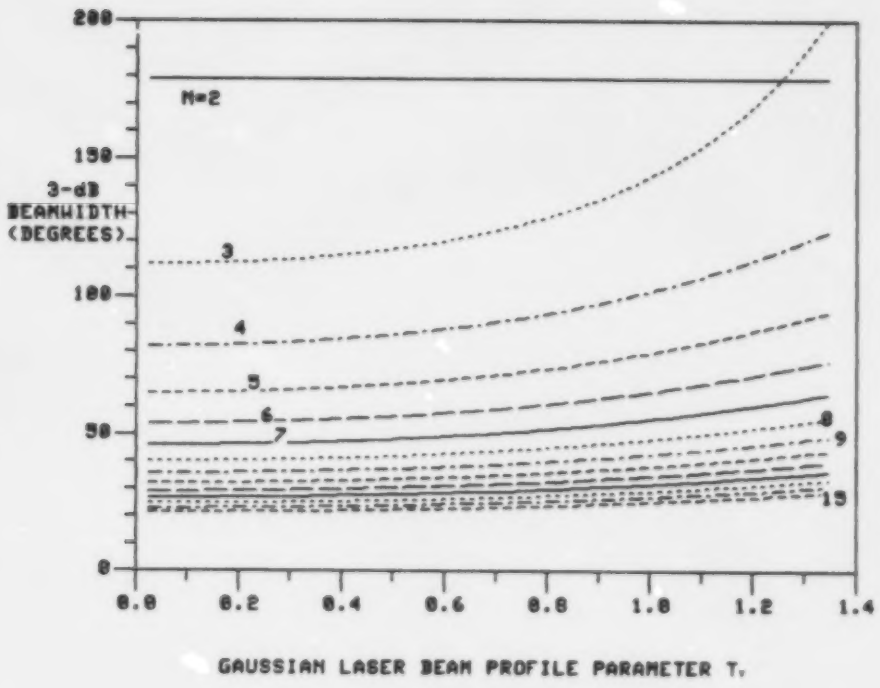

FIGURE 15: 3–dB BEAMWIDTH VERSUS Ty FOR A N–CHANNEL RECEIVER USING A CIRCULAR ANTENNA ARRAY ($H/\ell = 0.2$)

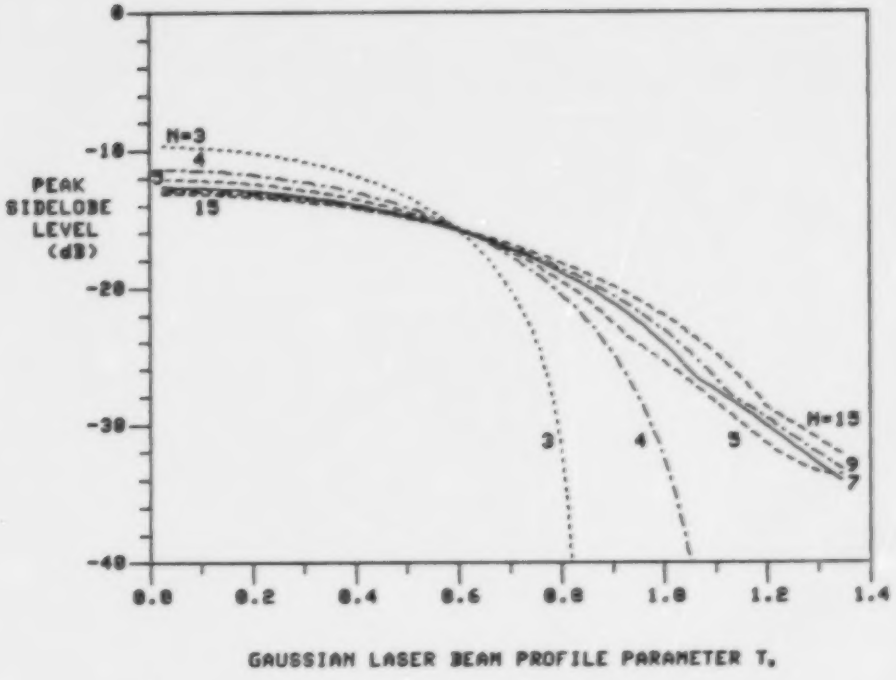

FIGURE 16: PEAK SIDELOBE LEVEL VERSUS Ty FOR A N–CHANNEL RECEIVER USING A CIRCULAR ANTENNA ARRAY ($H/\ell = 0.2$)

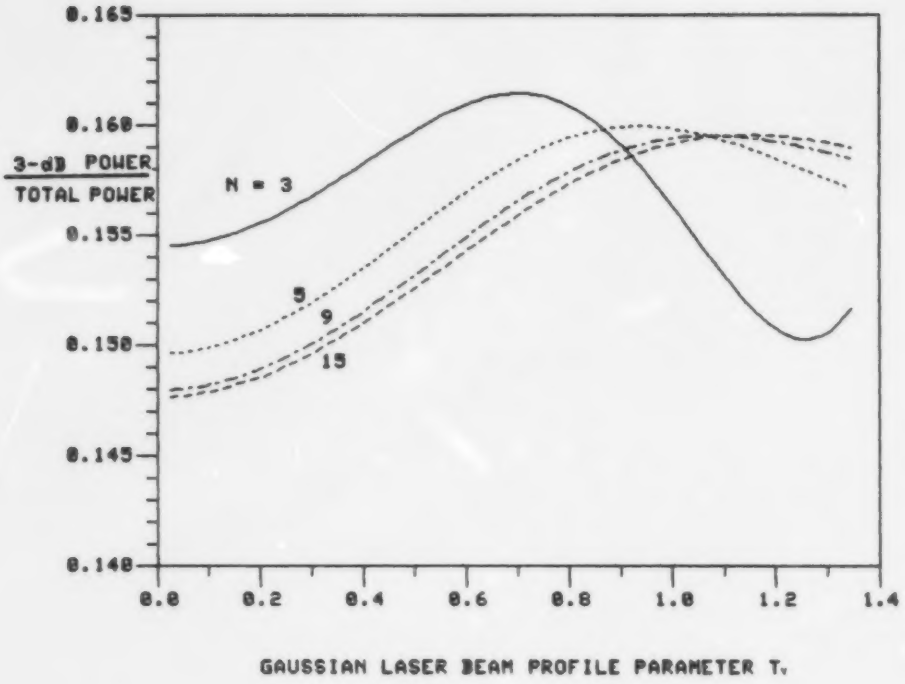

FIGURE 17: RATIO OF 3–dB BEAMWIDTH POWER TO TOTAL POWER VERSUS Ty FOR A N–CHANNEL RECEIVER USING A CIRCULAR ANTENNA ARRAY ($H/\ell = 0.2$)

where P.F. is the proportionality factor which is determined by the specific distribution of channel locations and weightings. For a given phase error, the pointing error is directly proportional to the proportionality factor and inversely proportional to the baseline length which increases by (N–1), where N is the number of channels. The P.F is plotted in Fig.18 as a function of Ty and is shown to increase with Ty. This is expected because the outer channels become less important as the weighting on them is reduced. As given in Eq.(102), the center channel located at the center of the array has no contribution to the P.F. In the case of N equals 3, the P.F. is the same as for N = 2 and the Gaussian weighting is found to have no effect on the outer two elements due to symmetry. From Fig. 18 and as pointed out in Section 8.2 for large N, the P.F. is approximately inversely proportional to the square root of N.

The normal processing carried out to determine DOA from such a system is by phase comparison between the various output ports. The finest accuracy is obtained by comparing the two channels with the largest phase difference but the result is ambiguous. This ambiguity is resolved by using the other channel pairs and a typical bearing accuracy of 2 degrees RMS can be achieved [47]. By using Eq.(100), a RMS phase error of 71 degrees is obtained. In the acoustooptic signal processor, all the channels are processed in parallel and as a result an improvement is expected. If the random phase error distribution in each output port is assumed to be the same but uncorrelated, then an improvement factor equals to 1.37 in bearing accuracy is obtained from Fig. 18 for Ty = 0. If this error is assumed to be much larger than the errors introduced by the rest of the system, a bearing accuracy of 1.5 degrees can be achieved using this particular processor. Moreover, this 2–D acoustooptic signal processor has the additional advantage of being able to process simultaneous signals.

The ideal DOA patterns as given in Figs.12 to 18 have been plotted by assuming there were no amplitude and phase errors. In practical system implementation, there are matching errors as described in Section 8. Using Eqs.(50) and Eq.(52), and for N = 9, the expected DOA patterns are given in Fig. 19 and Fig. 20 for Ty = 0 and 0.88 respectively. Ty = 0.88 is used because it produces a maximum output intensity as shown in Fig. 14,. They are plotted for various values of amplitude and phase errors. When Ty is not zero, there is a weighting on each channel and the amplitude error is weighted as well. As expected, the amplitude and phase errors raise the sidelobe levels and reduce the magnitude of the pattern. In addition, the errors reduce the effectiveness of amplitude weighting in suppressing the sidelobe levels.

The 2–D acoustooptic signal processor has been analyzed for a filled array configuration in this section. If there are channels missing from a filled array configuration, a degradation in performance is expected. The architecture as shown in Fig. 7 is used to illustrate the degradation effect when the output ports of ±3 are missing. The DOA patterns of both configurations are plotted in Fig.21 for Ty = 0.88 and $w/\ell = 0.2$. As can be seen from the graph, the sidelobe levels are much higher with a slight drop in the output main lobe level.

13.0 COMPARISON BETWEEN THE TWO CONFIGURATIONS

Both the linear antenna array and circular antenna array configurations have been analyzed in the previous sections and illustrated with design examples. In this section, unique features associated with each configuration are outlined and compared.

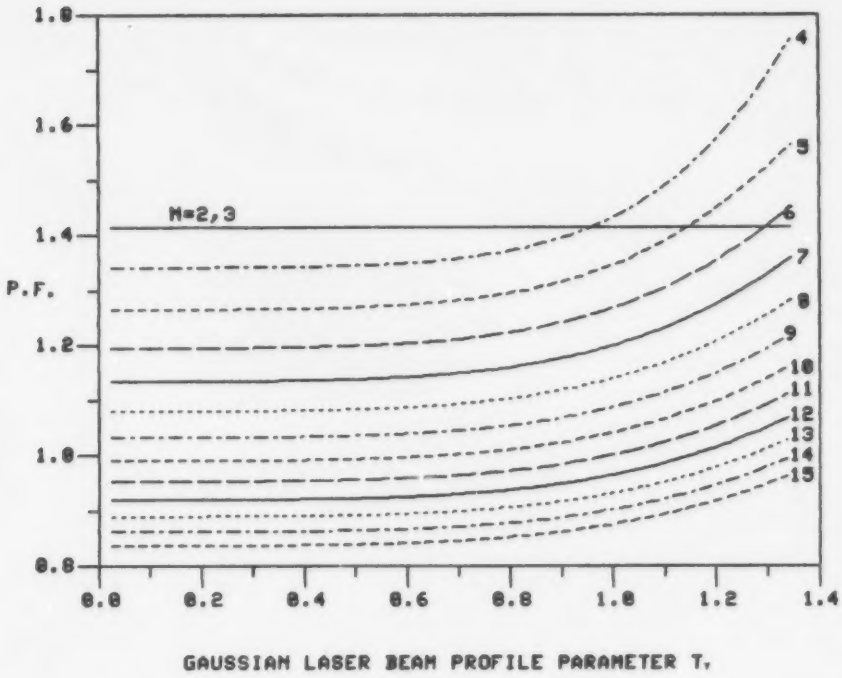

FIGURE 18: P.F. VERSUS Ty FOR A N–CHANNEL RECEIVER USING A CIRCULAR ANTENNA ARRAY ($H/\ell = 0.2$)

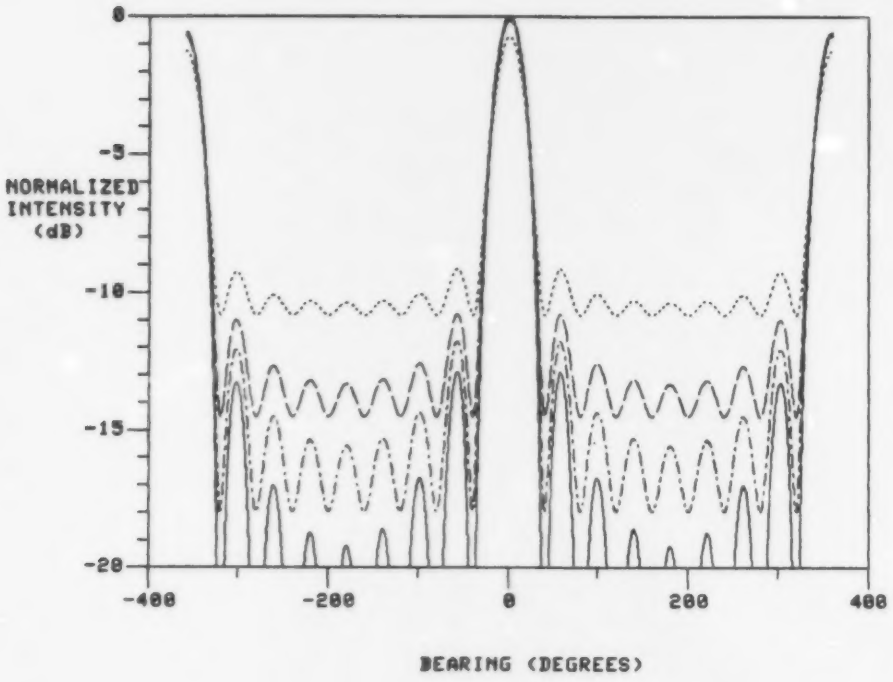

FIGURE 19: NORMALIZED DOA PATTERN OF A 9–CHANNEL RECEIVER USING A CIRCULAR ANTENNA ARRAY FOR
Ty = 0 and $H/\ell = 0.2$
(a) ——— Error Free
(b) ····· 30° RMS Phase Error, –3 dB RMS Power Error
(c) – – – – – 15° RMS Phase Error, –6 dB RMS Power Error
(d) —·—·— 7.5° RMS Phase Error, –9 dB RMS Power Error

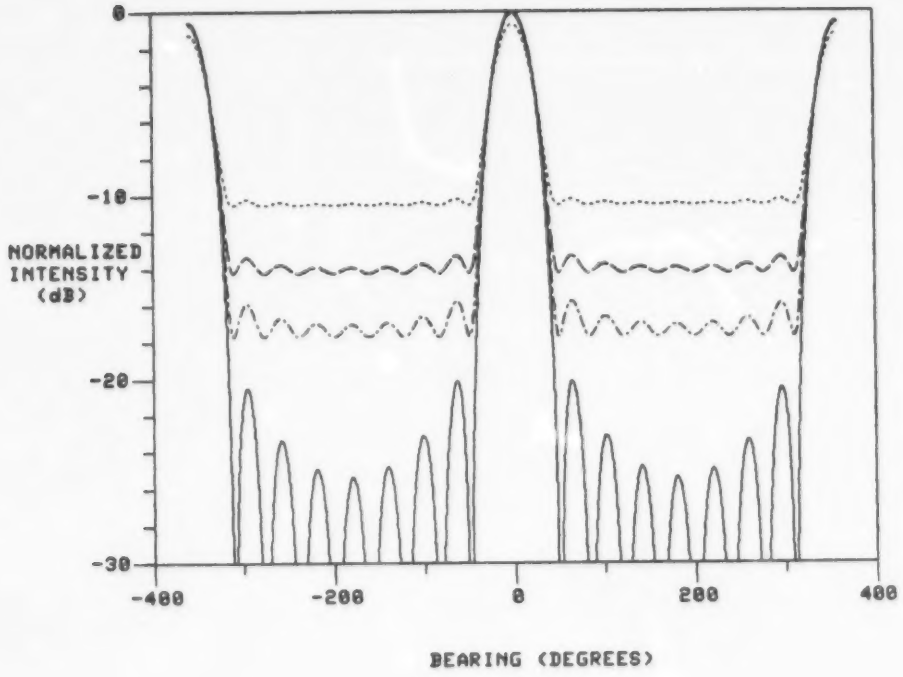

FIGURE 20: NORMALIZED DOA PATTERN OF A 9–CHANNEL RECEIVER USING A CIRCULAR ANTENNA ARRAY FOR OPTIMUM Ty = 0.88 and $H/\ell = 0.2$

(a) ——— Error Free
(b) ····· 30° RMS Phase Error, –3 dB RMS Power Error
(c) – – – – 15° RMS Phase Error, –6 dB RMS Power Error
(d) —·—·— 7.5° RMS Phase Error, –9 dB RMS Power Error

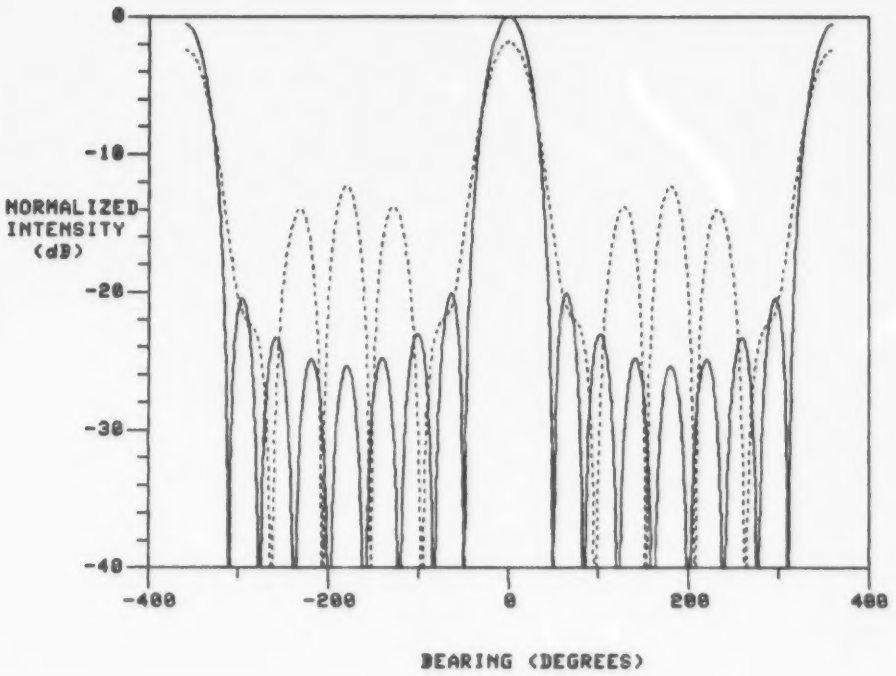

FIGURE 21: NORMALIZED DOA PATTERN OF A RECEIVER USING A CIRCULAR ANTENNA ARRAY FOR Ty = 0.88 and $H/\ell = 0.2$

(a) ———— 9–channel Filled Array

(b) ..... 7–channel Thinned Array

The 2–D acoustooptic signal processor using a linear antenna array was analyzed in detail and presented in Section 11. It was shown that an aperiodic array configuration with a minimum of four to five elements was useful for broadband receiver designs where it is required to cover an instantaneous angular field–of–view of one quadrant and with an angular accuracy of about one degree. This was based on factors such as complexity, cost, required main lobe beamwidth , sidelobe levels and antenna size constraint.

The antenna elements are arranged in a linear aperiodic array configuration and the multi–channel Bragg cell is also of the same arrangement. In using a linear antenna array , typically the instantaneous angular field–of–view of one quadrant (90–degree sector) can be achieved and in order to cover the full 360–degree instantaneous field–of–view, four identical receivers are needed.

In using a linear aperiodic array with only four to five antenna elements to cover an octave or more in frequency, the peak sidelobe–to–main–lobe levels are usually high, –2 to –3 dB (Fig. 9) for an angular accuracy in the order of one degree. More elements can be used to improve the level but with an increase in cost and complexity.

Using a linear antenna array to cover a broad frequency band, the baseline length of the antenna array when expressed in terms of the number of wavelengths changes with frequency. As a result the bearing information obtained in the Fourier plane by measuring the peak position of the DOA pattern has to be scaled by a scaling factor [Eq.(32)] which is directly proportional to the frequency of the signal. In addition, the DOA accuracy is also scaled by the same scaling factor.

For the design example of a 4–element transducer array configuration, the inter–transducer spacings required are much larger than the space occupied by the four acoustic transducers. If the multi–channel Bragg cell is uniformly illuminated with a laser beam, a great portion of the incident light will not be interacting with the acoustic beams even though there may be an appreciable spread in the acoustic beam profile (Fig. 11). This will reduce the amount of light diffracted with a corresponding loss in the sensitivity of such a receiver. A general solution is to use holographic lenses to split the input laser beam into a number of coherent beams to illuminate the acoustic beams. However, in additional to the complexity in generating and handling of holographic lenses, there are also losses and distortion introduced by these components.[48]

As outlined in Section 12, another approach in designing a 2–D acoustooptic signal processor is based on the circular antenna array with a Butler beamforming matrix. Some preliminary beamforming is carried out by the Butler matrix to convert the outputs of a circular array with a field–of–view of 360 degrees to a linear array output arrangement which can be used to feed a periodic multi–channel Bragg cell. Using this circular antenna array with a Butler matrix configuration, some attractive features can be identified when compared to the linear antenna array configuration:

(i) A full 360–degree instantaneous field–of–view can be achieved using only one 2–D acoustooptic signal processor.

(ii) The peak sidelobe–to–main–lobe level can be improved by the use of amplitude weighting (Fig. 12).

(iii) The shift in the DOA pattern as a function of input azimuthal angle is independent of frequency [Eq.(62)] and as a result both the accuracy and resolution of this processor are also independent of frequency.

(iv) Since the transducers of the multi–channel Bragg cell are in a periodic arrangement, the inter–transducer spacings can be reduced considerably as compared to the aperiodic arrangement. The acoustic columns can now be illuminated fully without the use of a beam–shaping optics such as holographic lenses. If we assume the ratio of the transducer width to inter–transducer spacing is 1 to 3 and for a Gaussian illumination profile truncated at the $1/\exp(3.125)$ points for a 9–channel configuration, then the maximum through–put loss is 5 dB as compared to 12 dB for the 4–element aperiodic array.

Despite the advantages associated with the circular antenna array configuration, the aperiodic linear array configuration does offer some good features. For the same number of channels, an aperiodic arrangement will provide a longer baseline and all those features associated with it such as better bearing accuracy. There may be lower cross–talks among those channels further apart. In addition the microwave front–end will be less complicated and much smaller in size which will result in a lower cost. However when the elevation angle is not zero ,the bearing accuracy may deteriorate due to "Coning" angle problems [22–23].

The ultimate choice depends on the specific system requirement. The circular array configuration can provide a system which is more compact and simpler if the full 360–degree instantaneous field–of–view is required. The bearing accuracy is moderate, on the order of 1 degree with a 9–channel system. For angular accuracy of better than 1 degree, the linear array configuration is a better choice if the errors associated with the "Coning" angle can be solved by either measuring the elevation angle using another system or by operating the system for very low elevation coverage.

14.0 SUMMARY AND CONCLUSIONS

2–D acoustooptic signal processors, for simultaneous DF and spectrum analysis of radar signals over a wide instantaneous bandwidth, have been shown to be of great potential for Radar ESM applications.

A comprehensive treatment on the analysis and design of 2–D acoustooptic signal processors has been provided in this report. Two general 2–D acoustooptic architectures have been analyzed: one using a linear antenna array, and the other using a novel architecture based on a circular antenna array with a Butler matrix beamformer.

Emphasis has been placed on the DF characteristics of both architectures. For the linear antenna array configuration, the optical deflection angle of the DOA pattern is directly proportional to a scaling factor and the sine of the bearing. The scaling factor is found to be directly proportional to the input RF frequency. For the circular antenna array configuration, the optical deflection angle is directly proportional to the bearing and a scaling factor which is independent of frequency.

An error tolerance analysis has also been carried out on the 2–D processors. The dominant effect of amplitude and phase errors on the DOA pattern is a reduction in gain and a change in the main–lobe–to–sidelobe ratios. For a given phase tracking error, the pointing error is inversely proportional to the array length and the specific spatial distribution of the weighted channels. For N large, it is approximately inversely proportional to the square root of the number of channels (N). For the linear antenna array configuration, it is also inversely proportional to the cosine of the bearing.

There are no "invisible" regions in the DOA array pattern as for the antenna array pattern. In addition, for the linear antenna array configuration, the shape of the DOA array pattern is unchanged when the signal arrives off boresight.

For a given acoustic array arrangement of a multi–channel Bragg cell, the peak DOA pattern is a function of the Gaussian laser illumination profile parameter Ty. A maximum output is achieved by the appropriate choice of the parameter Ty. However, the maximum in the peak DOA pattern usually may not result in a maximum in terms of the total optical power interacting with the acoustic beams. As a result, maximizing the total interacting power may have no significance in terms of maximizing the output DOA pattern.

The optical light distribution from the 2–D acoustooptic signal processor is detected by using a time–integrating 2–D photodetector array. The effect due to the transformation by the processor on the DOA pattern for input dominant RF noise and a CW signal has been extended from a single–channel configuration to a N–channel one. For low input signal–to–noise ratio, the output signal–to–noise ratio for a single–channel configuration, is directly proportional to the product of the time–bandwidth product and the square of the effective input signal–to–noise ratio. For the N–channel configuration, the effective input signal–to–noise ratio is modified by N times the square of the normalized array factor and thus the maximum output signal–to–noise ratio is improved by a factor of N^2 and the processing gain is N.

A typical example has been presented to illustrate some optimization techniques on the design of a 2–D acoustooptic signal processor using a linear antenna array. It is shown that an aperiodic array configuration with a minimum of four to five elements is useful for broadband receiver designs where it is required to cover an instantaneous angular field–of–view of one quadrant and with an angular accuracy of about one degree. This is based on factors such as complexity, cost, required main lobe beamwidth , sidelobe levels and antenna size constraint. However, the peak sidelobe–to–main–lobe level is usually high, –2 to –3 dB. In addition, the shift in the DOA pattern and DOA accuracy are scaled by the same scaling factor.

Another approach in designing a 2–D acoustooptic signal processor is based on the circular antenna array with a Butler beamforming matrix. Some preliminary beamforming is carried out by the Butler matrix to couple the output from a circular array to a multi–channel Bragg cell of a periodic arrangement. A typical example using a 32–element circular antenna array and a Butler matrix with 9 output ports has been given and a bearing accuracy of 1.5 degrees can be achieved . Design characteristics, such as peak sidelobe level, relative DOA pattern intensity, proportionality factor and main beamwidth, as a function of the Gaussian illumination parameter Ty and the number of channels have also been investigated. Some attractive features which can be identified when compared to the linear antenna array configuration are:

(i) A 360–degree instantaneous field–of–view can be achieved,
(ii) the DOA pattern is simpler and both the accuracy and resolution are independent of frequency and,
(iii) due to periodic arrangement, the peak sidelobe–to–main–lobe level can be effectively reduced by the use of amplitude weighting and
(iv) the throughput loss is less when the multi–channel Bragg cell is illuminated fully.

The ultimate choice of configuration is dependent on the specific system requirement. The circular array configuration provides a system which is more compact if 360–degree instantaneous field–of–view is required. The bearing accuracy is moderate on the order of 1 degree with a 9–channel system. For angular accuracy of better than 1 degree, the linear array configuration is a better choice if the " Coning" angle problem can be eliminated.

15.0 REFERENCES

[1] "Special Issue on Electronic Support Measures " IEE Proceedings–F, Communications, Radar and Signal Processing, Vol 132, Part F, Number 4, July 1985.

[2] D. Casasent and D. Psaltis, "Classification for Optical Signal Processing Architectures", in Proceedings, Acoustooptic Bulk Wave Devices, pp. 32–38, SPIE, Monterey, 1979.

[3] T.M. Turpin, "Spectrum Analysis Using Optical Processing", Proceedings of the IEEE. Vol. 69, No. 1, pp. 79–92,Jan, 1981.

[4] D.L. Hecht, "Spectrum Analysis Using Acoustooptic Devices", Optical Engineering, Vol. 16, No.5 ,pp. 461–466, Sept./Oct. 1977.

[5] L.B. Lambert, M. Arm and A. Aimette, "Electro–optical Signal Processors for Phased Array Antennas", in Optical and Electro–optical Information Processing, J.T. Tippet et al., Eds., Chapter 38, pp. 715–748, MIT Press, Cambridge 1965.

[6] A.E. Spezio," Acousto–optics for Electronic Warfare Applications ", Proceedings: 12 Annual Aeilomar Conference on Circuits, Systems and Computers pp.596–608, 1978.

[7] R.A. Coppock and R.F. Croce, "Wideband Optical Channelizer for Simultaneous Frequency and Direction Finding", in Proceedings, Acoustooptic Bulk Wave Devices (SPIE, Monterey, 1979), pp. 124–129.

[8] J.P.Y. Lee, " Interferometric Acoustooptic Signal Processor for Simultaneous Direction Finding and Spectrum Analysis ", Applied Optics, Vol. 22, No.6, pp. 867–872, 15 March 1983.

[9] J.P.Y. Lee, " Two–dimensional Acoustooptic Signal Processor Using a Circular Antenna Array and a Butler Matrix ", DREO Tech. Memo.TM 27/87, Oct, 1987.

[10] J.W. Goodman, Introduction to Fourier Optics, McGraw–Hill, New York, 1968.

[11] A. Korpel, Acoustooptics , Marcel Dekker Inc. New York,1988.

[12] E.I. Gordon, "A Review of Acoustooptical Deflection and Modulation Devices", Proc. IEEE,Vol. 54, No. 10, pp.1391–1401, Oct. 1966.

[13] R. Adler, "Interaction Between Light and Sound", IEEE Spectrum, pp.42–54, May 1967.

[14] I.C.Chang, "Acoustooptic Devices and Applications", IEEE Trans. Sonics Ultrason., Vol. SU–23, No.1, pp.2–22, Jan. 1976.

[15] J. P.Y. Lee, " Acoustooptic Fourier Transforming Configuration for Spectrum Analysis and Determination of Direction–of–Arrival", Ph.D Thesis, Dept of Electronics, Carleton University, Ottawa, Nov 1986.

[16] R.W. Dixon, "Acoustic Diffraction of Light in Anisotropic Media", IEEE Journal of Quantum Electronics, Vol. QE–3, No.2, pp. 85–93, Feb. 1967.

[17] A. Vander Lugt, "Bragg cell Diffraction Patterns", Applied Optics, Vol. 21, No. 6, pp. 1092–1100, 15 March 1982.

[18] D.L. Hecht, "Three Dimensional Acoustooptic Dispersion Effects in Acoustooptic Devices for Optical Information Processing", IEEE Ultrasonics Symposium 1983, pp. 463–466.

[19] D.L. Hecht and G.W. Petrie,"Acoustooptic Diffraction from Acoustic Anisotropic Shear Modes in Gallium Phosphide", IEEE Ultrasonics Symposium 1980, pp. 474–478.

[20] J.E.B. Oliveira, E.L. Adler, D. Souilhac and A.A Gundjian, " Acoustooptic Diffraction and Deflection in Tellurium at 10.6 μm", IEEE Ultrasonics Symposium 1984, pp. 332–340.

[21] J.P.Y. Lee, To be published

[22] L.G. Bullock, G.R. Oeh and J.J. Sparagna, " An Analysis of Wide–band Microwave Monopulse Direction–Finding Techniques", IEEE Trans. Aerospace and Electronic Systems, Jan 1971, Vol. AES–7, No.1 pp. 188–203.

[23] D. W. Horner, " Specification, Calibration and Testing of Phase Interferometers ", Microwave Journal, Feb 1988.

[24] " Digital ESM Receivers with High D/F Accuracy ", Anaren Microwave, Pub. M1826–18.

[25] B. Sheleg, " A Matrix–Fed Circular Array for Continuous Scanning", Proc. IEEE Vol. 56, No. 11, pp. 2016–2027, November 1968.

[26] J.P.Y. Lee, "Acoustooptic Spectrum Analysis of Radar Signals Using an Integrating Photodetector Array", Applied Optics, Vol. 20, No. 4, pp.595–600, 15 Feb. 1981.

[27] D.C. Sinclair and W. Earl Bell, Gas Laser Technology, Holt, Rinehart and Winston,Inc., 1969.

[28] A.H. Firester, T.E. Gayeski and M.E. Heller,"Efficient Generation of Laser Beams with an Elliptic Cross Section", Applied Optics, Vol.11, No.7, pp.1648–1649, July 1972.

[29] W. Veldkamp and E. Van Allen, "Compact, Collinear, and Variable Anamorphic–beam Compressor Design", Applied Optics, Vol. 21, No.1, pp.7–9, 1 Jan. 1982.

[30] B.D. Steinberg, Principles of Aperture and Array System Design ,Wiley, New York, 1976.

[31] Fairchild Charge Coupled Device Catalog, "CCD, The Solid State Imaging Technology", Palo Alto, Ca., 1982–1983.

[32] Reticon Product Summary, "Solid–State Image Sensors", 64 to 2048 elements, Reticon Corp., Sunnyvale,Ca., 1979.

[33] G.M. Borsuk, "Photodetectors for Acoustooptic Processors", Proc. IEEE, Vol. 69, No. 1, pp. 100–118, Jan. 1981.

[34] S.G Chamberlain and J.P.Y. Lee, "A Novel Wide Dynamic Range Silicon Photodetector and Linear Imaging Array", in IEEE Trans. on Electron Devices, Vol. ED–31, No.2, pp. 175–182, Feb. 1984 and IEEE Journal of Solid–State Circuits, Vol. SC–19, No.1, pp.41–48, Feb. 1984.

[35] E.J. Boling and J.W. Dzimianski, " Monolithic Wideband Parallel Channel Detector Array" ,SPIE Vol.477, Optical Technology for Microwave Applications, 1984, pp.174–177.

[36] L.R. Hudson, C–R Chung, H–F Tseng, S.G Chamberlain and W.D. Washkurak, "High–speed High–Dynamic Range Linear Array", SPIE Vol. 972 Infrared Technology XIV, 1988 pp. 33–38

[37] P. Kellman, H.N. Shaver and J.W. Murray, "Integrating Acoustooptic Channelized Receivers", Proc. IEEE, Vol. 69, No.1 ,pp. 93–100, Jan. 1981.

[38] D. Psaltis and B.V.K. Vijaya Kumar, "Acoustooptic Spectral Estimation: A Statistical Analysis", Applied Optics, Vol. 20, No. 4, pp. 601–605, 15 Feb. 1981.

[39] K.A. Winick "Cramer–Rao Lower Bounds on the Performance of Charge–coupled–device Optical Position Estimators", J. Opt. Soc.Am.A, Vol.3, No.11/November 1986, pp 1809–1815.

[40] R.W. Schafer and L.R. Rabiner, "A Digital Signal Processing Approach to Interpolation", Proc. IEEE, June 1973, Vol. 61, No.6, pp. 692–702.

[41] M. Elbaum and P. Diament, "Estimation of Image Centroid, Size, and Orientation with Laser Radar", Applied Optics, Sept 1977, Vol. 16, No.9 pp. 2433–2437.

[42] H. Schjaer–Jacobsen and K. Madsen, "Synthesis of Nonuniformly Spaced Arrays Using a General Nonlinear Minimax Optimization Method", IEEE Trans. Antennas and Propagation, Vol. AP–24, No.4, pp.501–506, July 1976.

[43] M.I. Skolnik, "Nonuniform Arrays", Chapter 6 in Antenna Theory, Part I, Collin and Zucker Eds., McGraw–Hill, New York, 1969.

[44] J.P.Y. Lee, "Evaluation of the Experimental 2–D Acoustooptic Receiver", DREO Tech Memo TM 18/89, Sept, 1989.

[45] J.P.Y. Lee, "A Simple Phase–tracking Measurement Technique for Multi–channel Bragg Cells," Journal of Optical Engineering, Vol. 27, No.8, pp.667–683, August, 1988

[46] C–H Han, Y. Ishii and K. Murata,"Reshaping Collimated Laser Beams with Gaussian Profile to Uniform Profiles", Applied Optics, Vol.22, No.22, pp.3644–3647, 15 Nov.1983.

[47] "2–18 GHz, Digital ESM Receivers with 2 RMS Bearing Accuracy", Anaren Microwave, Pub. M1830–28.

[48] A. Vander Lugt, G.S. Moore and S.S. Mathe," Multichannel Bragg Cells: Compensation for Acoustic Spreading", Applied Optics, Vol. 22, No.23, pp. 3906–3912, 1 Dec. 1983.

APPENDIX

DERIVATION OF THE RMS BEAM–POINTING ERROR OF 2–D ACOUSTOOPTIC PROCESSORS

From Eq.(56), the intensity pattern is

$$f(v)f^*(v) = \frac{1}{N^2} \sum_{n=1}^{N} \sum_{m=1}^{N} a_n a_m \exp[-j(2\pi v \ell_{nm} - \delta\phi_{nm} - 2\pi\beta_{nm})] \tag{a1}$$

Making use of the property of odd symmetry in

$$\begin{aligned} \ell_{nm} &= -\ell_{mn} \\ \delta\phi_{nm} &= -\delta\phi_{mn} \\ \beta_{nm} &= -\beta_{mn} \end{aligned} \tag{a2}$$

and with the identity

$$\cos(x) = \left[\exp(jx) + \exp(-jx) \right] /2 \tag{a3}$$

Equation (a1) can be rewritten as

$$f(v)f^*(v) = \frac{1}{N^2} \sum_{n=1}^{N} \sum_{m=1}^{N} a_n a_m \cos(2\pi v \ell_{nm} - \delta\phi_{nm} - 2\pi\beta_{nm}) \tag{a4}$$

Let

$$v_o = \beta_{nm}/\ell_{nm} \tag{a5}$$

be the normalized position of the steered diffracted optical beam with no pointing errors and with a change of variable

$$v_1 = v - v_o, \tag{a6}$$

we have

$$f(v_1)f^*(v_1) = \frac{1}{N^2} \sum_{n=1}^{N} \sum_{m=1}^{N} a_n a_m \cos(2\pi v_1 \ell_{nm} - \delta\phi_{nm}) \tag{a7}$$

The pointing direction is found by setting the derivative of the above equation with respect to the variable v_1 to zero

$$\partial\Big[\, f(v_1) f^*(v_1) \Big] / \partial v_1 = 0$$

$$= \frac{2\pi}{N^2} \sum_{n=1}^{N} \sum_{m=1}^{N} a_n a_m \sin(2\pi v_1 \ell_{nm} - \delta\phi_{nm})\, \ell_{nm} \tag{a8}$$

Since the phase errors are assumed to be small, the pointing error also may be presumed to be small. With this assumption, the trigonometric term in Eq.(a8) is replaced by its argument, leading to

$$\frac{2\pi}{N^2} \sum_{n=1}^{N} \sum_{m=1}^{N} a_n a_m (2\pi v_1 \ell_{nm} - \delta\phi_{nm})\, \ell_{nm} = 0 \tag{a9}$$

Therefore,

$$\sum_{n=1}^{N} \sum_{m=1}^{N} 2\, a_n a_m\, \pi v_1 \ell_{nm}^2 = \sum_{n=1}^{N} \sum_{m=1}^{N} a_n a_m\, \ell_{nm} \delta\phi_{nm} \tag{a10}$$

and

$$2\pi v_1 = \frac{\sum_{n=1}^{N} \sum_{m=1}^{N} a_n a_m\, \ell_{nm} \delta\phi_{nm}}{\sum_{n=1}^{N} \sum_{m=1}^{N} a_n a_m\, \ell_{nm}^2} \tag{a11}$$

Only the phase difference term $\delta\phi_{nm}$ is a random variable. The expected value is zero because of the earlier assumption of zero mean phase errors. The second moment is

$$E(2\pi v_1)^2 = \frac{E\left[\sum_{n=1}^{N} \sum_{m=1}^{N} a_n a_m\, \ell_{nm} \delta\phi_{nm} \sum_{r=1}^{N} \sum_{p=1}^{N} a_r a_p\, \ell_{rp} \delta\phi_{rp} \right]}{\left[\sum_{n=1}^{N} \sum_{m=1}^{N} a_n a_m\, \ell_{nm}^2 \right]^2} \tag{a12}$$

The expected value of the numerator term is expanded to give

$$E\left[\sum_{n=1}^{N}\sum_{m=1}^{N}\sum_{r=1}^{N}\sum_{p=1}^{N} a_n a_m a_r a_p \ell_{nm}\ell_{rp}\delta\phi_{nm}\delta\phi_{rp}\right]$$

$$= E\left[\sum_{n=1}^{N}\sum_{m=1}^{N}\sum_{r=1}^{N}\sum_{p=1}^{N} a_n a_m a_r a_p (\ell_n-\ell_m)(\ell_r-\ell_p)\right.$$

$$\left.(\delta\phi_n\delta\phi_r - \delta\phi_n\delta\phi_p - \delta\phi_m\delta\phi_r + \delta\phi_m\delta\phi_p)\right] \qquad \text{(a13)}$$

There are four $\delta\phi$ product terms in Eq.(a13) and let's consider the first product term

$$E\left[\sum_{n=1}^{N}\sum_{m=1}^{N}\sum_{r=1}^{N}\sum_{p=1}^{N} a_n a_m a_r a_p (\ell_n-\ell_m)(\ell_r-\ell_p)\delta\phi_n\delta\phi_r\right] \qquad \text{(a14)}$$

There are four product terms in the above equation and they are zero except when indices are common. Therefore

$$E(\delta\phi_n\delta\phi_r) = 0 \quad , \text{for } n \neq r \qquad \text{(a15)}$$

and

$$E(\delta\phi_n\delta\phi_n) = \sigma_\phi^2 \quad , \text{for } n = r \qquad \text{(a16)}$$

Making use of Eqs.(a15) and (a16) ,the solution for the numerator term is

$$E\left[\sum_{n=1}^{N}\sum_{m=1}^{N}\sum_{p=1}^{N} a_n^2 a_m a_p (\ell_n^2 - \ell_n\ell_p - \ell_m\ell_n + \ell_m\ell_p)\,\delta\phi_n\delta\phi_n\right]$$

$$= \sigma_\phi^2\left[\left(\sum_{n=1}^{N} a_n\right)^2 \sum_{n=1}^{N} a_n^2\ell_n^2 - 2\sum_{m=1}^{N} a_m \sum_{n=1}^{N}\sum_{p=1}^{N} a_n^2 a_p \ell_n\ell_p\right.$$

$$\left. + \sum_{n=1}^{N} a_n^2 \sum_{m=1}^{N}\sum_{p=1}^{N} a_m a_p \ell_m\ell_p\right] \qquad \text{(a17)}$$

Following a similar analysis, the last three terms in Eq.(a13) yield the same solution as the first one and thus the expected second moment is

$$E(2\pi v_1)^2 = \left[2\pi\sigma_{v_1} \right]^2$$

$$= \left[4\sigma_\phi^2 \left[\left(\sum_{n=1}^{N} a_n \right)^2 \sum_{n=1}^{N} a_n^2 \ell_n^2 - 2 \sum_{m=1}^{N} a_m \sum_{n=1}^{N} \sum_{p=1}^{N} a_n^2 a_p \ell_n \ell_p \right.\right.$$

$$\left.\left. + \sum_{n=1}^{N} a_n^2 \sum_{m=1}^{N} \sum_{p=1}^{N} a_m a_p \ell_m \ell_p \right] \right] / \left[\sum_{n=1}^{N} \sum_{m=1}^{N} a_n a_m \ell_{nm}^2 \right]^2 \qquad \text{(a18)}$$

and the normalized optical RMS beam–pointing error is then given by

$$\sigma_{v_1} = \sigma_\phi \left[\left(\sum_{n=1}^{N} a_n \right)^2 \sum_{n=1}^{N} a_n^2 \ell_n^2 - 2 \sum_{m=1}^{N} a_m \sum_{n=1}^{N} \sum_{p=1}^{N} a_n^2 a_p \ell_n \ell_p \right.$$

$$\left. + \sum_{n=1}^{N} a_n^2 \sum_{m=1}^{N} \sum_{p=1}^{N} a_m a_p \ell_m \ell_p \right]^{1/2} / \left[\pi \sum_{n=1}^{N} \sum_{m=1}^{N} a_n a_m \ell_{nm}^2 \right] \qquad \text{(a19)}$$

This is a general solution which takes into account the element weighting as well as the arbitrary locations of the elements.

UNCLASSIFIED

SECURITY CLASSIFICATION OF FORM
(highest classification of Title, Abstract, Keywords)

DOCUMENT CONTROL DATA

(Security classification of title, body of abstract and indexing annotation must be entered when the overall document is classified)

1. ORIGINATOR (the name and address of the organization preparing the document. Organizations for whom the document was prepared, e.g. Establishment sponsoring a contractor's report, or tasking agency, are entered in section 8.)

NATIONAL DEFENCE
DEFENCE RESEARCH ESTABLISHMENT OTTAWA
SHIRLEY BAY, OTTAWA, ONTARIO K1A 0Z4 CANADA

2. SECURITY CLASSIFICATION (overall security classification of the document including special warning terms if applicable)

UNCLASSIFIED

3. TITLE (the complete document title as indicated on the title page. Its classification should be indicated by the appropriate abbreviation (S,C or U) in parentheses after the title.)

2-D ACOUSTO-OPTIC SIGNAL PROCESSORS FOR SIMULTANEOUS SPECTRUM ANALYSIS AND DIRECTION-FINDING (U)

4. AUTHORS (Last name, first name, middle initial)

JIM P. LEE

5. DATE OF PUBLICATION (month and year of publication of document)	6a. NO. OF PAGES (total containing information. Include Annexes, Appendices, etc.)	6b. NO. OF REFS (total cited in document)
NOVEMBER 1990	83	48

7. DESCRIPTIVE NOTES (the category of the document, e.g. technical report, technical note or memorandum. If appropriate, enter the type of report, e.g. interim, progress, summary, annual or final. Give the inclusive dates when a specific reporting period is covered.)

DREO REPORT

8. SPONSORING ACTIVITY (the name of the department project office or laboratory sponsoring the research and development. Include the address.)

NATIONAL DEFENCE
DEFENCE RESEARCH ESTABLISHMENT OTTAWA
SHIRLEY BAY, OTTAWA, ONTARIO K1A 0Z4 CANADA

9a. PROJECT OR GRANT NO. (if appropriate, the applicable research and development project or grant number under which the document was written. Please specify whether project or grant)	9b. CONTRACT NO. (if appropriate, the applicable number under which the document was written)
011LB11	

10a. ORIGINATOR'S DOCUMENT NUMBER (the official document number by which the document is identified by the originating activity. This number must be unique to this document.)	10b. OTHER DOCUMENT NOS. (Any other numbers which may be assigned this document either by the originator or by the sponsor)
DREO REPORT 1049	

11. DOCUMENT AVAILABILITY (any limitations on further dissemination of the document, other than those imposed by security classification)

(X) Unlimited distribution
( ) Distribution limited to defence departments and defence contractors; further distribution only as approved
( ) Distribution limited to defence departments and Canadian defence contractors; further distribution only as approved
( ) Distribution limited to government departments and agencies; further distribution only as approved
( ) Distribution limited to defence departments; further distribution only as approved
( ) Other (please specify):

12. DOCUMENT ANNOUNCEMENT (any limitation to the bibliographic announcement of this document. This will normally correspond to the Document Availability (11). However, where further distribution (beyond the audience specified in 11) is possible, a wider announcement audience may be selected.)

UNCLASSIFIED

SECURITY CLASSIFICATION OF FORM

DCD03 2/06/87

UNCLASSIFIED

SECURITY CLASSIFICATION OF FORM

13. ABSTRACT (a brief and factual summary of the document. It may also appear elsewhere in the body of the document itself. It is highly desirable that the abstract of classified documents be unclassified. Each paragraph of the abstract shall begin with an indication of the security classification of the information in the paragraph (unless the document itself is unclassified) represented as (S), (C), or (U). It is not necessary to include here abstracts in both offical languages unless the text is bilingual).

(U) 2-D Fourier transforming acoustooptic signal processors, for simultaneous direction finding (DF) and spectrum analysis of radar signals over a wide instantaneous bandwidth, are shown to be useful for Radar Electronic Support Measures (ESM) applications A comprehensive treatment on the analysis and design of two general 2-D acoustooptic architectures is provided. In one architecture, a linear antenna array is employed, and in the other a novel circular antenna array with a Butler matrix beamformer is used. Emphasis is placed on the DF characteristics of both architectures. The effects of scaling factor, acoustic transducer height, Gaussian laser illumination profile, RF input noise, amplitude and phase tracking errors on the DOA pattern produced by each architecture are addressed. Design criteria and comparison between the two architectures are also provided.

14. KEYWORDS, DESCRIPTORS or IDENTIFIERS (technically meaningful terms or short phrases that characterize a document and could be helpful in cataloguing the document. They should be selected so that no security classification is required. Identifiers, such as equipment model designation, trade name, military project code name, geographic location may also be included. If possible keywords should be selected from a published thesaurus. e.g. Thesaurus of Engineering and Scientific Terms (TEST) and that thesaurus-identified. If it is not possible to select indexing terms which are Unclassified, the classification of each should be indicated as with the title.)

UNCLASSIFIED

SECURITY CLASSIFICATION OF FORM